UNIVERSITY OF PÉCS

Doctoral School of Physics

Nonlinear optics and spectroscopy program

Investigations into high energy THz and ultra-broadband IR radiation from organic salt crystal emitters

PhD thesis

Balázs Monoszlai

Supervisors:
Dr. József András Fülöp
Senior research fellow
University of Pécs

Prof. Dr. Christoph Peter Hauri
Group Leader
Paul Scherrer Institute

PÉCS, 2017

Table of Contents

1. Preface

I have completed the Doctoral School and wrote this dissertation at the Institute of Physics, Faculty of Science, University of Pécs (Hungary). Research for this thesis was performed at the Laser Group of SwissFEL at Paul Scherrer Institute (Switzerland) during my exchange program.

Nowadays cutting-edge scientific research has become too complex and difficult to be efficiently a single-person's work. Most of the results are considered to be a group effort, and therefore in this writing the common passive voice structure has been used instead of the first person singular which is traditionally used in Hungarian thesis.

My personal activity in the topic of this dissertation is primarily based on experimental lab-work and data evaluation. However theoretical simulations and calculations are an integral part of this scientific work therefore have also included to maintain continuity. The main contributor has been explicitly stated where I had none or minimal input to a certain part of the work.

2. Introduction

THz radiation is a band of electromagnetic radiation which is located between microwaves and infrared radiation. It is actually a “relatively” new name for the high frequency microwaves and far infrared radiation bands. This frequency range is also used to known as the THz gap, due to the lack of efficient generation and detection techniques. Radio and microwaves at the lower frequency end have been routinely generated with electronic techniques and optical techniques provided efficient infrared radiation sources at the opposite end of the spectral range. Intense developments of the past two-three decades have resulted in THz radiation becoming routinely accessible and it has evolved to a widely researched scientific field.

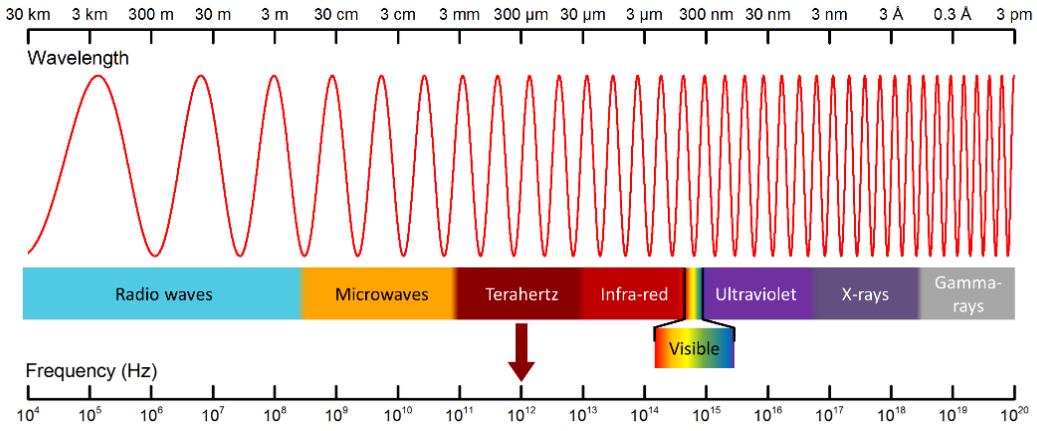

Figure 3.1.1 Location of the Terahertz band in the electromagnetic spectrum.

There are plenty of planned and realized applications of THz radiation used in several fields including industry, security and defense, medicine and last but not least scientific research. THz source development is the base of these studies and aims to gain the ability to create simple, easily available sources with high level of control over their parameters. Source development is still an ongoing, intensely developing part of THz

science. This thesis work will introduce a specific fraction of THz source development based on organic salt crystal emitters (OSC). The main topic here is the experimental characterization of a few OSCs to map different, mostly THz related properties and capabilities. Hopefully these results can contribute to the implementation and enhancement of future applications.

THz radiation can be used for non-invasive industrial quality check, as many nonmetallic materials are transparent in this spectral range. Thickness and layer structure of thin coatings including industrial paints, ceramics and plastics have been examined [1] [2] [3]. THz imaging is also a useful tool in the food industry as it is capable to detect different contaminations in food like glass or metal pieces or even organic ones e.g. insects [4] [5]. Other techniques like metallic detectors and x-ray imaging may not reveal all of these impurities.

Emitted radiation from rotational and vibrational transitions of molecules often falls into the THz regime. The molecule-specific spectral features are known as the spectral fingerprint. It can be used for identification of concealed substances in mails and parcels without opening them [6]. THz imaging is used also for security checks to detect hidden objects like melee weapons, firearms or explosives [7]. It can be applied safely on people, as THz radiation is non-ionizing radiation due to its low photon energy.

THz radiation is also used in medicine, mainly to detect and localize melanoma and other type of cancers on skin and in surrounding tissues up to a couple of millimeters depth [8] [9]. THz radiation is strongly absorbed by liquid water and thus it can be an excellent and sensitive tool for cornea hydration measurements via reflectometry techniques [10].

The application opportunities of THz radiation in science are also extremely versatile. It can be used for time-domain spectroscopy in linear and nonlinear regimes to determine a sample's absorption and dispersion with a simple measurement (Chapter 3.3.2). Time resolved techniques are suitable for observing induced dynamics in the irradiated materials in THz pump—optical probe or THz pump—THz probe setups [11]. Resonant and non-resonant control over matter has also been demonstrated in different materials and structures including the motion of free electrons, rotations and orientation of molecules, vibrations of crystal lattices and precessions of spins [12] [13] [14]. At higher THz field strengths, the effective manipulation of charged particles – primarily electron(beam) acceleration, undulation, deflection, spatial and temporal focusing – become available [15]. This interaction could enhance the high-harmonic generation based attosecond-pulse generation by introducing asymmetry in the laser-ionized electron trajectories [16] [17]. The operation of a THz-driven electron gun has been demonstrated recently [18] and apparently it has multiple advantageous properties when compared to conventional electron guns. THz-driven electron acceleration has been also demonstrated [19], which could one day become a cost-effective alternative for conventional large-scale accelerator facilities.

3. Theoretical overview

3.1. General overview of THz sources

This chapter gives brief descriptions of several different THz sources which have been developed over the years, based on different physical phenomena, starting with continuous THz emitters with narrow spectral bandwidth, followed by the pulsed THz emitters with broad spectral bandwidth. Organic salt crystals are introduced in a separate Chapter (3.2) due to their prominent place.

Far-Infrared (organic) molecular gas lasers

Molecular gas lasers are based on the transitions between rotational modes of molecules e.g. ammonia, methanol, fluoromethane, difluoromethane and are continuous emitters [20]. They have several narrow spectral bandwidths which usually lay in the 0.2-8 THz range [21]. In principle, their assembly are identical to optically excited gas lasers with an extra intracavity waveguide to limit transversal cavity modes. Their output power is typically in the range of tens-to-hundreds of milliwatts [21].

Backward wave oscillator

A backward wave oscillator (Figure 3.1.1) is an electron vacuum tube with an internal metallic grating structure which induces spatial modulation of the longitudinal electric field, driving the electron beam into bunches [20]. These bunches excite surface waves on the electrically conducting grating. Coherent energy transfer occurs when there is velocity matching between bunches and surface waves. The electron speed can be tuned by the bias voltage between the anode and cathode and thus the wavelength of the generated electromagnetic waves can be also controlled. Under certain conditions, present in

backward wave oscillators, the group velocity of the surface waves is negative and thus the energy transferred to the field is transported and amplified in the backward direction [20]. Electromagnetic radiation is coupled out of the tube using a waveguide.

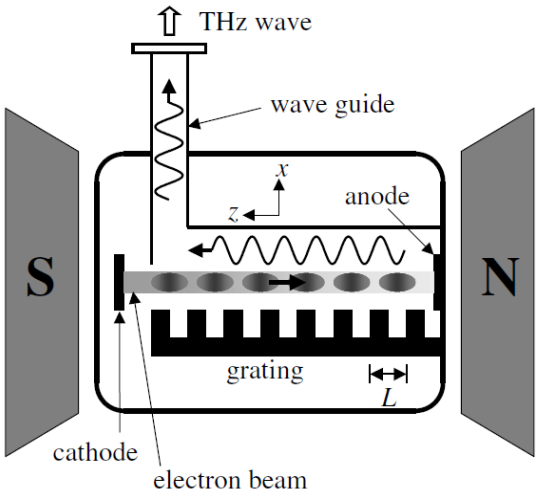

Figure 3.1.1 Schematic diagram of backward wave oscillator. [20]

The frequency of the generated electromagnetic waves is typically in the range of 0.03-1 THz [22]. The entire spectral range can be covered by roughly ten different tubes as each tube can be tuned around ~10 % of its central frequency. The output power is about 100 mW for frequencies below 200 GHz, diminishing to ~1 mW as the operation the operation frequency increase to 1 THz.

Quantum cascade laser

Quantum cascade lasers (QCL) are compact semiconductor lasers which emit in the mid- and far-infrared regions [20] [23] [24]. They consist of several periods of different semiconductor layers forming a superlattice. Typical (interband) semiconductor lasers emit photons due to recombination of electron-hole pairs across the material band gap. QCLs operate via intersubband transitions. The superlattice act as a series of one-dimensional quantum wells (Figure 3.1.2). The electrons move from one semiconductor

layer to another through the injection barriers via tunneling. Matching the electron wave functions in adjacent layers is important as it controls the feed rate. The electrons experience a three-level system with population inversion at the active regions (intersubband transitions) and lasing occurs due to the continuous electron flow through the layers. These systems are extremely efficient as the electrons emit photons in each period (cascading) [25].

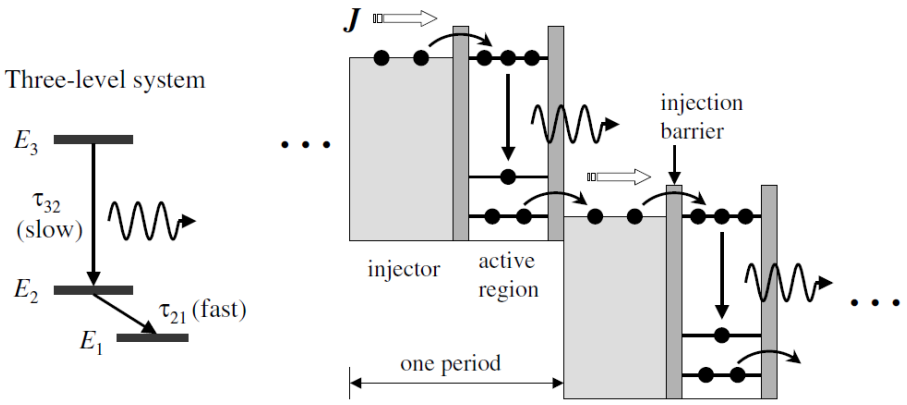

Figure 3.1.2 Schematic illustration of lasing and cascading in a QCL superlattice structure [20].

In case of too small differences among intersubband energy levels – like at THz QCLs – the population inversion can be spoiled by the temperature of the system thus they require cryogenic cooling. There are several developments to overcome this problem and achieve easier operation conditions at higher temperatures like 200-225 K [26] [27], but up to now they can operate only at low powers.

QCLs typically have narrow bandwidths and are continuous or “quasi” continuous emitters, typically operating in single- or multi-mode depending on the temperature, applied material and cavity type. THz QCLs can cover the 1-5 THz [24] frequency range and their output power can exceed 100 mW average power [28] in continuous and 1 W peak

power [29] in pulsed mode. Recently, short THz pulses with couple of picoseconds duration from mode-locked QCLs have been demonstrated [30] [31] [32].

Free electron laser

Free electron lasers (FELs) use relativistic electrons to generate monochromatic radiation from microwaves to x-rays [20]. They belong to the large scale facilities but THz FELs with exceptionally high >100 W output power can be realized with moderated sizes as they require low-energy electrons [33] [34]. Electrons are accelerated to relativistic speed then passed through an undulator which introduce a transverse sinusoidal modulation in their trajectory via Lorentz force. The charged particles are under acceleration and thus emit photons. The most effective operation mode of FELs is the superradiant mode when the electron bunches are shorter than the radiation wavelength. In such case the generated electromagnetic radiation is highly coherent and the photon-gain is greater than other operation modes [35]. The wavelength of an FEL depends on the wiggler period, the magnetic field strength and the electron beam energy and thus is tunable within a certain range. THz regime FELs can cover a broad frequency range of 0.88-100 THz [20].

Gas plasma

THz radiation can be produced with photo-generated plasma, in ambient air or noble gases [36]. The widely used technique is based on focusing and mixing ultrashort laser pulses with the fundamental frequency ω and its second-harmonic at frequency 2ω (Figure 3.1.3). The free electrons of the laser-induced plasma create a subpicosecond directional current due to the driving force of the asymmetric two-color laser field, giving rise to THz radiation [37] [38] [39].

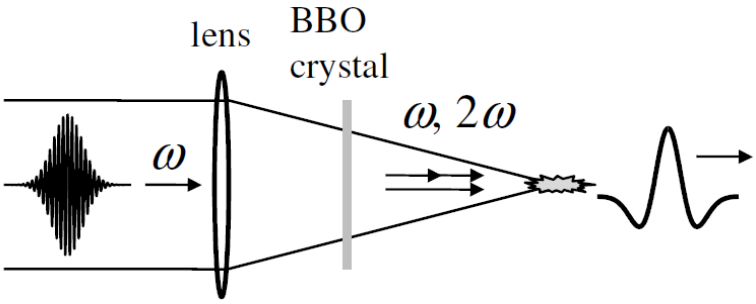

Figure 3.1.3 Experimental setup schematic of the 2-color field induced THz generation [20].

This simple setup can be optimized by varying pulse energy, relative phase between the fundamental and its second-harmonic field, length of the plasma filament, gas type and pressure [40]. The use of cylindrical lens can result in larger interaction volume and results in pulse energies up to 7 μJ and conversion efficiency greater than 10^{-4} [41] [42]. Ultrashort pumping pulses (32 fs) generates extreme spectral bandwidth from 0.5 THz to 35 THz [43].

Gas plasma can be also used to detect THz pulses through the process of four-wave mixing. In order to the improve the dynamic range and ensure coherent detection, an external alternating bias can be applied around the focal points of the interacting THz and fundamental probe beams. In such case the detection technique is called the THz air-biased-coherent-detection (THz-ABCD) [44]. The intensity of the generated second-harmonic is proportional to THz electrical field strength and bias field strength therefore the average terahertz amplitude in the detection region can be determined from the measurement [43]. The temporal waveform of the THz pulses can be mapped out by varying the delay between the THz and fundamental probe pulses (Chapter 3.3.2).

Photoconductive antennas

Photoconductive (PC) antennas are electrical switches utilizing the photo-generated free carriers in semiconductors [20]. They are capable to emit or detect THz radiation as the switching action in the PC antenna can occur in the subpicosecond time range. The switch-on time is a function of the exciting laser pulse duration, while the switch-off time is mainly determined by the lifetime of photo-excited carriers. The most commonly used materials for THz emitters and detectors are radiation-damaged silicon-on-sapphire (RD-SOS) and low-temperature grown gallium arsenide (LT-GaAs) [20].

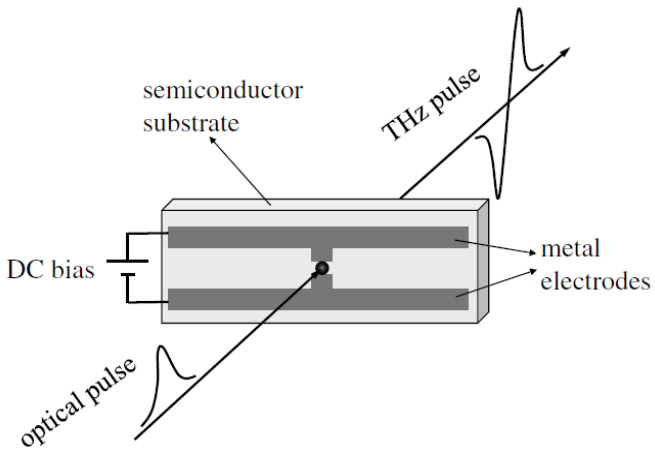

Figure 3.1.4 Schematic diagram of THz pulse emission from a PC antenna excited by a femtosecond laser pulse [20]

PC antenna THz emitters have two metal electrodes deposited on a semiconductor substrate (Figure 3.1.4) with a DC bias. Femtosecond optical pulses with photon energy larger than the bandgap of the semiconductor generate free electron and hole pairs in the gap between the electrodes [20]. The static electric field accelerates the free carriers, but at the same time their number is decreasing primarily by trapping in defect sites. The impulse current arising from the acceleration and the decay of free carriers is the source of the single-cycle subpicosecond pulses of electromagnetic radiation. The radiation is highly divergent as the size of the source is much smaller than the THz wavelength. The

standard solution for this problem is a lens directly attached to the backside of a PC emitter which significantly reduces the divergence of the THz radiation.

The power and bandwidth of the emitted THz can dramatically vary and also depends on the substrate material, the metal electrode structure, the bias voltage and the optical pump power. The maximum radiation power is limited by the breakdown voltage of the substrate material. The newly developed high-power PC antennas can reach the mW power level [45], but most of them operate at the tens-hundreds of μW level. They usually pumped by a femtosecond oscillator or a fiber laser at high repetition rate. They can cover the 0.1-4 THz range [46].

The DC voltage source connected to the electrodes must be replaced by a sensitive current meter for THz detection. In the absence of a bias field, the THz electric field induces current in the photoconductive gap if the photo-generated free carriers are injected by the optical probe pulse [20]. The optical pulse acts as a fast gating, which can be used to scan the temporal waveform of the THz pulses (Chapter 3.3.2).

Optical rectification in nonlinear crystals

During light-matter interactions in most of the cases the key interaction occurs between the electromagnetic waves and the electrons. The electromagnetic waves force electrons to move, and the accelerated motion of electrons induces electromagnetic radiation [20]. During these forced movements, the electron distribution rearranges and produces charge separation inside of the atoms and molecules, thus the material becomes polarized. At low intensities, the *P(t)* induced polarization of the material is proportional to the *E(t)* driving electric field strength and can be described as

$$P(t) = \epsilon_0 \chi^{(1)} E(t), \qquad \text{(3.1.1) [47]}$$

where ϵ_0 is the permittivity of free space and $\chi^{(1)}$ is the linear susceptibility.[1] Eq. (3.1.1) has to be generalized for higher electric field strengths to keep its validity, which is possible by expanding *P(t)* in a power series:

$$\begin{aligned} P(t) &= \epsilon_0 \left[\chi^{(1)} E(t) + \chi^{(2)} E^2(t) + \chi^{(3)} E^3(t) + \cdots \right] \\ &\equiv P^{(1)}(t) + P^{(2)}(t) + P^{(3)}(t) + \cdots, \end{aligned} \qquad \text{(3.1.2) [47]}$$

where $\chi^{(n)}$ and $P^{(n)}(t)$ are the higher (*n*-th) order nonlinear susceptibility and nonlinear polarization respectively for $n>1$. For condensed matter the typical value of linear susceptibility $\chi^{(1)}$ is on the order of unity whereas the second- ($\chi^{(2)}$) and third-order ($\chi^{(3)}$) nonlinear susceptibilities are in the order of ~10^{-12} m/V and ~10^{-24} m^2/V^2 respectively [47]. Eq. (3.1.2) shows that the linear term dominates at low field strengths, but as the field strength is increasing, the higher order terms are become comparable and give rise to different nonlinear processes.

If electromagnetic waves with two distinct frequencies are considered within a condensed material with non-zero second order susceptibility, the second order nonlinear polarization can be expressed as:

$$\begin{aligned} P^{(2)}(t) = \epsilon_0 \chi^{(2)} \big[& E_1^2 e^{-2i\omega_1 t} + E_2^2 e^{-2i\omega_2 t} + 2E_1 E_2 e^{-i(\omega_1+\omega_2)t} + \\ & 2E_1 E_2^* e^{-i(\omega_1-\omega_2)t} + c.c. \big] + 2\epsilon_0 \chi^{(2)} [E_1 E_1^* + E_2 E_2^*], \end{aligned} \qquad \text{(3.1.3) [47]}$$

where each term of the expression describes a second order optical process such as second-harmonic generation (SHG), sum-frequency generation (SFG), difference-frequency generation (DFG) and optical rectification (OR) [47] [48] [49] [50] [51].

[1] Quantities simplified to scalars and assumed that the medium responds instantaneously thus it is also lossless and dispersion-free.

The most important term for THz generation is the last one from Eq. (3.1.3), namely the OR. It can be considered as a special case of DFG, where the interaction occurs among the frequency components of a spectrally broad electromagnetic pulse [47]. The typically applied pump pulse durations for THz generation via OR are in the range of tens to hundreds of femtoseconds. The short laser pulses can provide access to high intensities where the nonlinear processes are effective and their spectral bandwidth can cover the range up to ~20 THz.

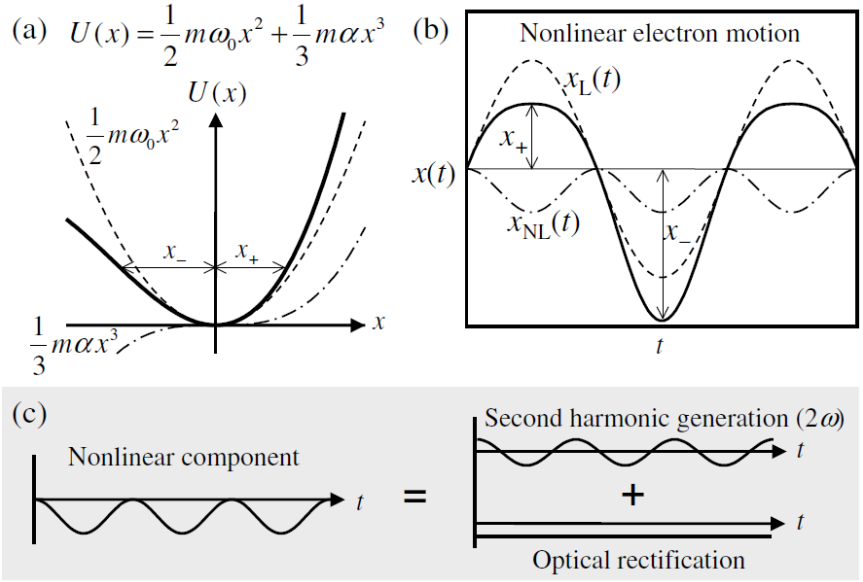

Figure 3.1.5 (a) The electric potential energy and (b) the nonlinear motion for an electron in a noncentrosymmetric medium. (c) Shows the nonlinear motion component and it's elements [20]

OR like any other second-order nonlinear optical process can only occur in noncentrosymmetric crystals [47]. In case of nonlinearities of electronic origin, the diverse electronegativity of different kind of atoms leads to uneven charge distribution thus asymmetric potential energy along the molecular axis (Figure 3.1.5 (a)). When the applied field is strong enough, easily achievable with laser fields, the discrepancy between the positive ($x+$) and negative ($x-$) electron displacements becomes substantial (Figure 3.1.5

(b)) [20]. This anharmonic motion is composed from the original linear/harmonic motion and a new nonlinear component which can be further split to OR and SHG (Figure 3.1.5(c)).

Phase matching means no more than maintaining a proper phase relationship between the interacting waves during propagation. When the Δk wavevector mismatch is close to zero, the coherent energy transfer is constructive among the waves and it results in an effective nonlinear interaction [47]. In such case the I_{NL} intensity of a second-order nonlinear optical process is proportional to the phase mismatch factor:

$$I_{NL} \propto sinc^2\left(\frac{\Delta k\, L}{2}\right), \qquad (3.1.4)\ [47]$$

where L is the interaction length in the nonlinear media.

In the case of THz generation via OR, the THz phase velocity and the pump group velocity have to be matched. This can be achieved via different techniques like birefringent phase matching [52] [53], quasi-phase matching [54] [55] or tilted pulse front technique [56] since the refractive indices are usually different at the pumping infrared and at the THz wavelengths.

Semiconductors like ZnTe, GaP, GaAs are often used versatile materials in THz technology. They can be used as photoconductive antenna substrates (Chapter 3.1) or as nonlinear crystals either for THz generation/detection. In the linear regime they are optically isotropic crystals. Simple collinear phase matching is possible for ZnTe, GaP and GaAs at 0.8 µm, 1 µm and 1.35 µm pump wavelengths respectively [20], as the refractive indices are similar at the IR [57] [58] [59] and THz ranges [60] [61] [62]. Their nonlinear coefficients are not exceptional. In the case of ZnTe and GaAs their values are d_{eff}=68.5 and 65.6 pm/V respectively, meanwhile the coefficient of GaP reaches only d_{eff}=24.8 pm/V [63] [64]. Fortunately around their operation frequencies they possess low

THz absorption, in the range of α_{THz}=0.5 to 1.9 cm^{-1} [60] [63] [65]. These properties make them considerable THz sources in the low-energy range. Their spectrum typically cover the low/middle range of THz frequencies between 0.1-3 THz and their pulse energies are at the sub-μJ–μJ levels with energy conversion efficiencies less than 10^{-4} [66]. Their main limitation originates from the strong two photon absorption at the common pump wave lengths. It influences the maximal useful pump intensity and the generated free carriers in the semiconductor material also increase the THz absorption [67]. There are recent promising solutions for that problem using longer pump wavelength and tilted pulse front technique [68]. Enhanced THz generation has been demonstrated with pulse energies up to 14 μJ and conversion efficiency up to 0.7% [69] [70].

Lithium niobate (LN) is one of the most popular nonlinear crystals for high-intensity THz generation. Both the congruent and stoichiometric forms can be used and cm sized crystal can be grown. LN has a tendency to accumulate defects in the crystal structure during growth leading to unwanted photorefractive effect and consequently damage at high-intensity exposures. A small level of magnesium-oxide doping (0.5-6 %) can help to suppress the photorefractive effect and increase the damage threshold up to 100 GW/cm^2 levels [71] [72]. LN is a birefringent crystal, but the large refractive index difference between the pumping-infrared (n=2.15 and n_{group}=2.2 at 1030 nm) and THz (n_{THz}=4.96 at 1 THz) ranges excludes the opportunity of birefringent phase matching [72] [73] [74]. Thus an effective phase matching like tilted pulse front technique is indispensable for efficient THz generation via OR. LN has a high effective nonlinear coefficient of d_{eff}=168 pm/V for THz generation [64]. Unfortunately this is coupled also with a relatively high THz absorption coefficient of α_{THz}=17 cm^{-1} at 1 THz, which can be reduced to less than its 30 % by cryogenic cooling of the crystal [72] [74] [75]. LN sources typically cover the low

frequency part of the THz range between 0.1-1.5 THz. Their pulse energies can achieve tens to hundreds of μJ with typical conversion efficiencies around ~1 % [76] [77].

3.2. Organic salt crystals as THz sources

This group of crystals consist of organic compounds and some of them own extremely high nonlinear properties. They can be used for both THz generation via optical rectification and THz detection via electro-optic effect. The most well-known organic salt crystal (OSC) types are the DAST, DSTMS, OH1, HMQ-TMS and BNA crystals. Although some of their properties are similar, they possess different characteristics. Their typical size is a couple of mm with few hundred μm thickness. They are strongly birefringent crystals, thus collinear phase matching for THz generation is possible over different IR wavelengths. They have several strong THz absorption peaks due to their complex molecule structure. The generated THz spectrum usually covers the range starting from 0.1 THz up to 3 THz or 5 THz but 15 THz has been also demonstrated [78] [79] [80]. The generated THz pulse energies are usually in the tens of μJ range as well an outstanding 0.9 mJ [81] has been also reported. The typical conversion efficiencies are around 1-3% at certain pumping wavelengths and intensity [79] [81].

3.2.1. DAST

The organic salt 4-N,N-dimethyl amino-4'-N'-methyl stilbazolium tosylate (DAST) crystals have been used for many years to generate THz radiation by optical rectification [82].

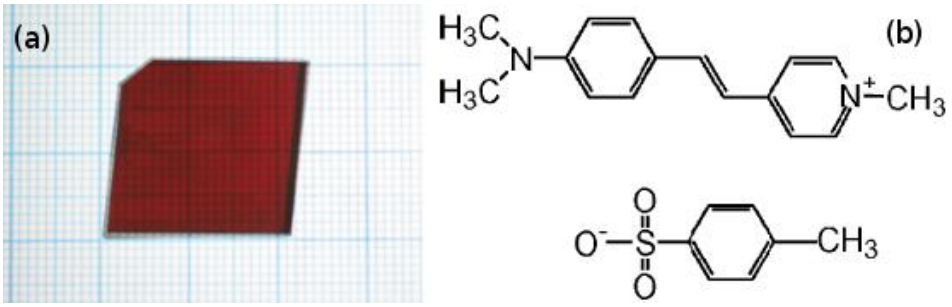

Figure 3.2.1 (a) Picture about a DAST crystal [83]. (b) Chemical structure of DAST [84].

The DAST crystal consists of cations with large molecular nonlinearity and anions to maintain the non-centrosymmetric packing – monoclinic space group Cc – in the crystalline phase [85]. The crystallographic *b*-axis coincides with the dielectric axis x_2 while the *a*- and *c*-axes differ from axes x_1 and x_3 by angles of 5.4° and 3.2°, respectively [86] [87]. In practical terms, those differences can be neglected.

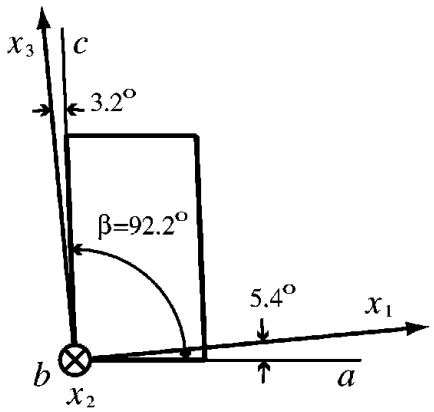

Figure 3.2.2 Arrangement of the crystallographic *a-, b-, c*-axes, and the dielectric x_1-, x_2-, and x_3-axes in DAST. [87]

DAST crystals can be produced from supersaturated methanol solution with concentration levels between 25 g/l and 45 g/l [88]. The initial nucleation in the solution can be enhanced with laser pulses in order to achieve better growth and quality [84]. The usual linear growth rates are in the range of 2 mm/month to 3 mm/day, depending on the applied method [89]. Crystals typically have 0.1-1 mm thickness, and 4-400 mm^2 area in the a-b plane (natural c-cut) [83] [86].

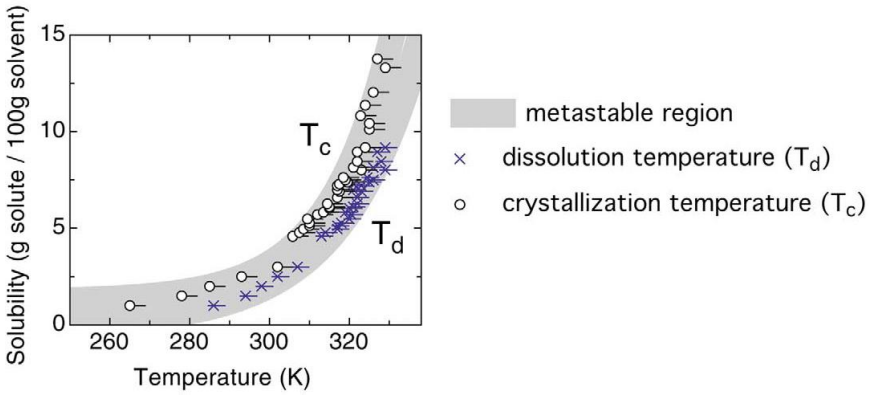

Figure 3.2.3 Solubility curve and metastable region of DAST in methanol. [89]

The n_i refractive indices of DAST in Figure 3.2.4 correspond to polarizations along the dielectric x_i axes. The high birefringence in the near infrared region is clearly observable. The absorption coefficients stay below 2 cm^{-1} for all polarization directions in region between 700 nm and 1650 nm [86]. Significant absorption peak is present only at shorter wavelengths between 390 nm and 570 nm [87] and dominates especially for polarizations along the dielectric x_1 axis. This absorption peak is responsible for the dispersion in the transparency region.

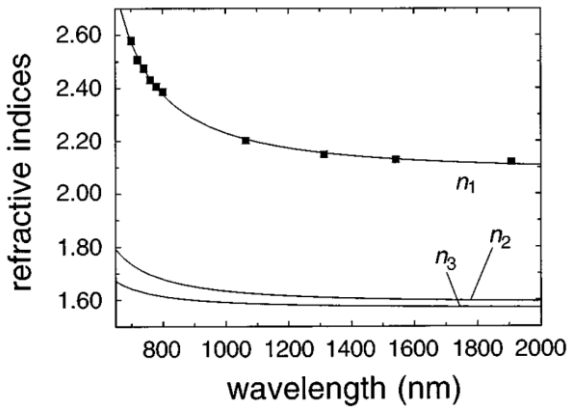

Figure 3.2.4 Refractive indices n_1, n_2, and n_3 of DAST as a function of the wavelength. The solid curves correspond to the Sellmeier dispersion formula [90].

The refractive index and absorption curves of DAST (Figure 3.2.5) become more diverse in the THz regime due to the complex molecule/crystal structure. The dielectric

function can be modeled using a series of Lorentz oscillators. In the 0.6-12 THz range 7-9 resonance peaks were observed with polarizations along *a*- and *b*- axes respectively [91]. The strongest and most important absorption peak – caused by a transverse optical phonon resonance– is located at 1.1 THz along the *a*-axis, and it has as great influence on the generated THz spectrum.

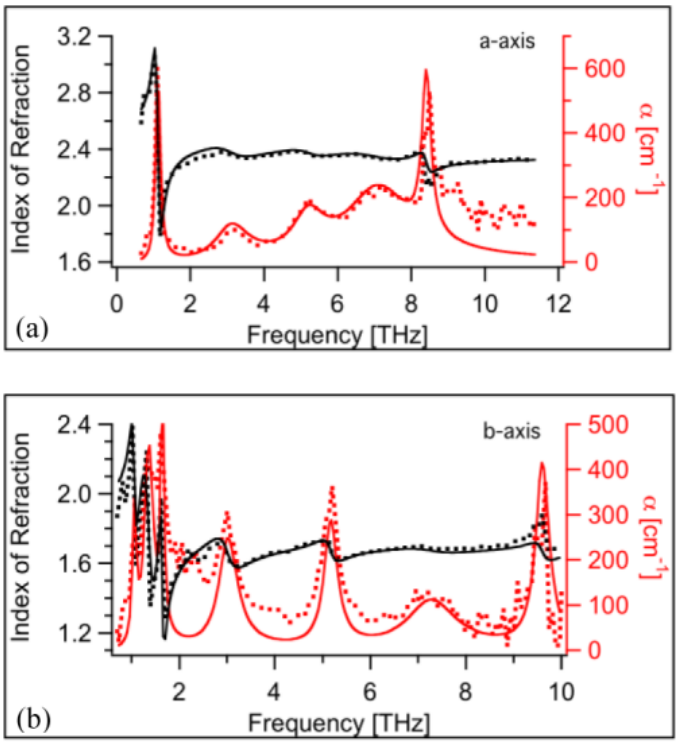

Figure 3.2.5 Refractive index and absorption coefficient of the (a) a- and (b) b-axis of DAST from 0.6 – 12 THz. The solid lines are fits to the Lorentz oscillator model [91].

The DAST crystals are usually pumped in normal incidence for THz generation. The similarity of refractive indices at the near infrared (Figure 3.2.4)[2] and THz ranges (Figure 3.2.5) besides the length of THz wavelengths allows to maintain sufficient phase matching over hundreds of µm co-propagation. A pump beam polarized along the *a*-axis is suitable

[2] Shown values are simple refractive indices and not the group indices which are relevant for phase matching.

for longer wavelengths around 1500 nm, while a beam polarized along the *b*-axis is proper for shorter wavelengths around 800 nm.

The crystal symmetry of DAST permits 14 non-zero r_{ijk} electro-optic coefficient and 4 of them are bigger than 1 pm/V [86] [90]. Their related χ_{ijk}^{OR} nonlinear susceptibilities for optical rectification (Table 3.2.1) can be calculated by

$$\chi_{ijk}^{OR}(\omega, \omega_{THz}) = -\frac{1}{2} n_j^2(\omega) n_k^2(\omega) r_{jki}(\omega, \omega_{THz}), \qquad (3.2.1)\ [85]$$

where n_j and $n_k$represent the refractive indices along the dielectric *j* and *k* axes respectively. The largest tensor element χ_{111}^{OR} at 800 nm has an outstandingly high 1230±130 pm/V value, but unfortunately it cannot be used for THz generation due to strong phase mismatch. Around 1535 nm where the phase matching is given, its value decreased by a factor of 2.5, but it still has a remarkable 490±90 pm/V value which provides efficient THz generation.

Wavelength	$\boldsymbol{r_{111}}$	$\boldsymbol{r_{221}}$	$\boldsymbol{r_{113}}$	$\boldsymbol{r_{122}}$
800 nm	77±8	42±4	15±2	17±1.5
1535 nm	47±8	21±4	5±1	-
	$\boldsymbol{\chi_{111}^{OR}}$	$\boldsymbol{\chi_{122}^{OR}}$	$\boldsymbol{\chi_{311}^{OR}}$	$\boldsymbol{\chi_{212}^{OR}}$
800 nm	1230±130	**166±16**	239±32	135±12
1535 nm	**490±90**	69±13	52±10	-

Table 3.2.1 The largest electro-optic coefficients r_{ijk} and nonlinear susceptibilities χ_{kij}^{OR} of DAST [86] [90]. All tensor elements are in units of **pm/V**.

3.2.2. DSTMS

The outstanding nonlinear properties of DAST crystals, has resulted in other organic salt crystals being developed by molecular engineering. Roughly one decade ago a new, promising DAST derivative was presented: 4-N,N-dimethylamino-4'-N'-methyl-stilbazolium 2,4,6-trimethylbenzenesulfonate (DSTMS).

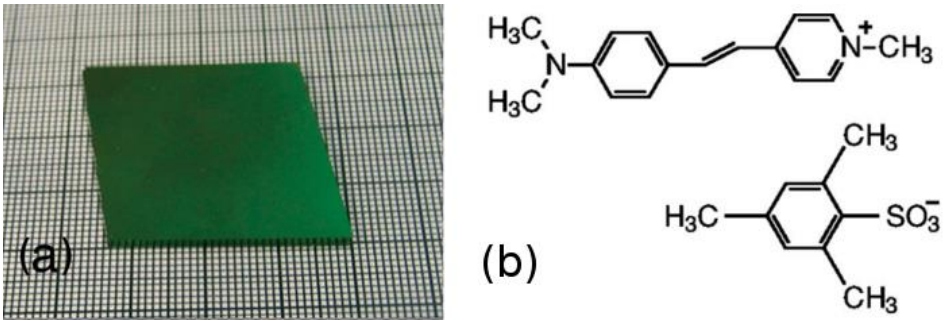

Figure 3.2.6 (a) Picture about a DSTMS crystal [92]. (b) Chemical structure of DSTMS [93].

The molecular and crystal structure of DSTMS is very similar to those of DAST. The anions of DSTMS have 2 extra methyl groups (Figure 3.2.1 and Figure 3.2.6). The positive and negative ions form non-centrosymmetric packing which belongs to the monoclinic space group Cc [93]. Despite these extra methyl groups, the crystallographic *b*-axis still coincides with the dielectric axis x_2 whereas the *a*-axis deviates from x_1 by angle of 3.6±0.3°.

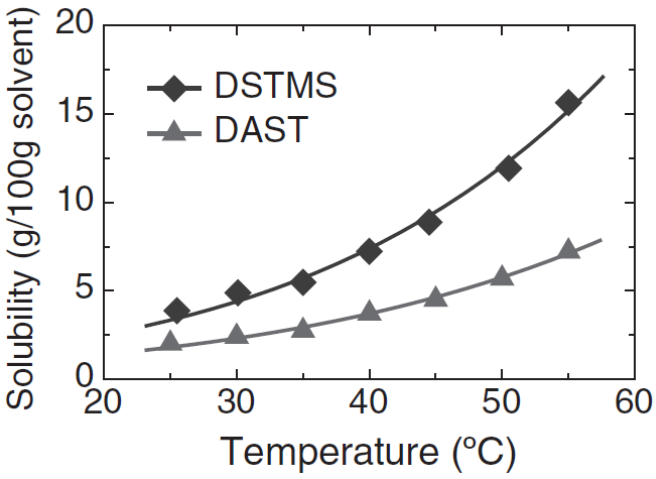

Figure 3.2.7 Solubility/temperature curves of DSTMS and DAST in methanol [92].

Figure 3.2.7 shows that DSTMS is about 2 times more soluble in methanol than DAST. The driving force of crystallization strongly depends on the achieved level of supersaturation [94]. It is possible to obtain very large – up to 400 mm^2– bulk single crystals and thin films with good optical quality without using seed crystals [92] [95]. Growing high quality single crystals of DSTMS with surface area of about 1 cm^2 is possible within 2 weeks, 2-3 times faster than DAST.

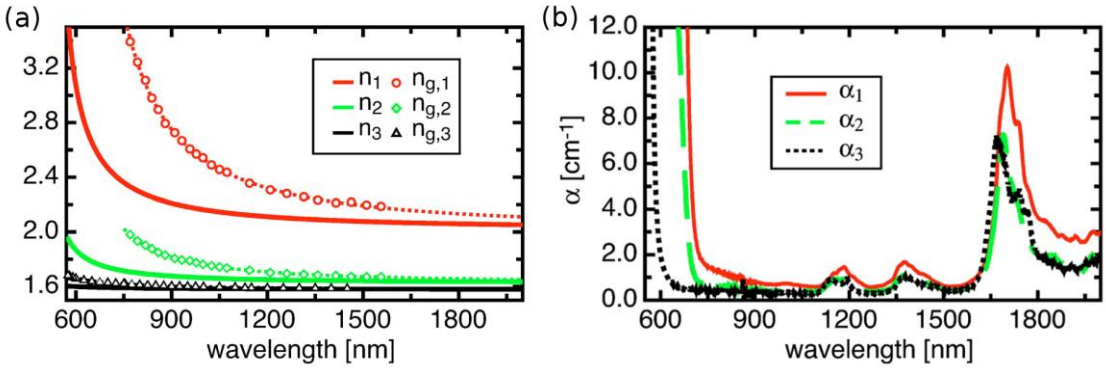

Figure 3.2.8 (a) Group indices $n_{g,1}$ (circles), $n_{g,2}$ (diamonds),and $n_{g,3}$ (triangles) of DSTMS as a function of the wavelength. The solid curves are the corresponding dispersion relations of the refractive indices n_1, n_2, and n_3 respectively. (b) Absorption coefficients α_1 (solid curve), α_2 (dashed curve) and α_3 (dotted curve) of DSTMS as a function of the wavelength [93]

The n_i refractive indices and $n_{g,i}$ group indices of DSTMS in Figure 3.2.8 (a) correspond to polarizations along the dielectric x_i axes (*i=1, 2, 3*). Like DAST, DSTMS also

shows high birefringence in the near-infrared region. The absorption coefficients – Figure 3.2.8 (b) – stay below 2 cm^{-1} for all polarization directions in region between 700 nm and 1600 nm. Outside of this region the absorption increases significantly [93].

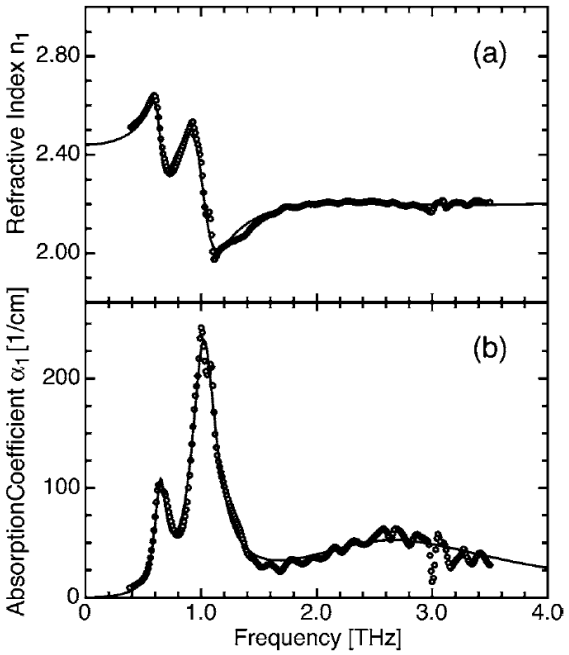

Figure 3.2.9 (a) Refractive index $n_1(\omega)$ and (b) the absorption coefficient $\alpha_1(\omega)$of DSTMS in the THz range. Open circles: measured data. Curves: theoretical functions, including three harmonic oscillators [96].

The refractive indices of DSTMS (Figure 3.2.9 (a)) and DAST (Figure 3.2.5(a)) are similar in the THz range for polarizations along x_1 dielectric axis [96] with larger differences of the absorption coefficients. DSTMS has reduced absorption coefficient by ~60% average compared to DAST and the strongest resonance peak is shifted to 0.96 THz.

Data about the second order nonlinear susceptibility of DSTMS for OR is only available for 1907 nm pump wavelength. Its value is $\chi_{111}^{OR} = 430 \pm 40$ pm/V [92] which is close to DAST at this wavelength $\chi_{111}^{OR} = 420 \pm 110$ pm/V [97]. Based on several

similarities between DAST and DSTMS, it can be expected that there will be comparable nonlinear properties at other wavelengths too.

3.3. THz detection

3.3.1. Power/Energy measurements

Bolometers

Bolometers are thermal detectors which use materials with temperature sensitive resistivity [98]. They can measure radiation power with high sensitivity over an exceptionally wide spectral range from THz to X-rays [20].

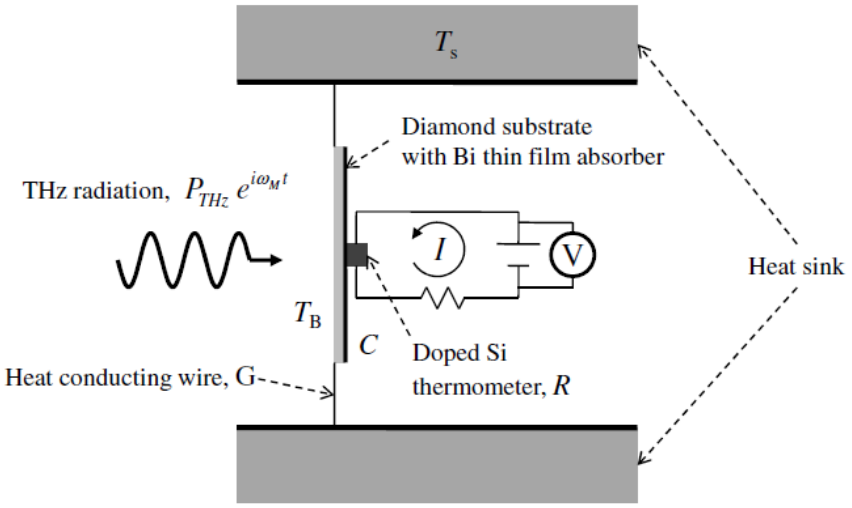

Figure 3.3.1 Schematic diagram of a typical composite bolometer. Where P_{THz} is the incident THz power modulated at the angular frequency ω_M. The thermometer is characterized by the temperature-dependent resistance R. C is the heat capacity of the absorber/substrate/thermometer unit. T_B is the substrate temperature. G is the dynamic thermal conductance of the heat conducting wire connecting the substrate to the heat sink. The bias V varies to keep the current I, flowing through the thermometer, constant. [20]

Modern bolometers are composite bolometers as they consist of several independently optimized components to achieve better performance in general (Figure 3.3.1). A radiation absorber and a temperature sensitive resistance are deposited on a substrate with good

thermal conductivity. [20] The substrate is connected to a heat sink by heat conducting wires. The heat sink usually includes a liquid helium dewar to maintain the temperature of detector in the cryogenic ranges. The irradiated energy is converted into heat, which raises the temperature of the absorber and thermometer assembly. This induces a change in the thermometer resistance, detected by measuring the change of the current flowing through it.

Pyroelectric detectors

Pyroelectric crystals are spontaneously polarized crystals, each unit cell has a permanent electric dipole moment, aligned with a specific crystal axis [20]. The level of this spontaneous electric polarization is depends on the temperature and this physical phenomenon is called pyroelectricity. The spontaneous polarization is accompanied by surface charge, neutralized by free carriers forming a steady state.

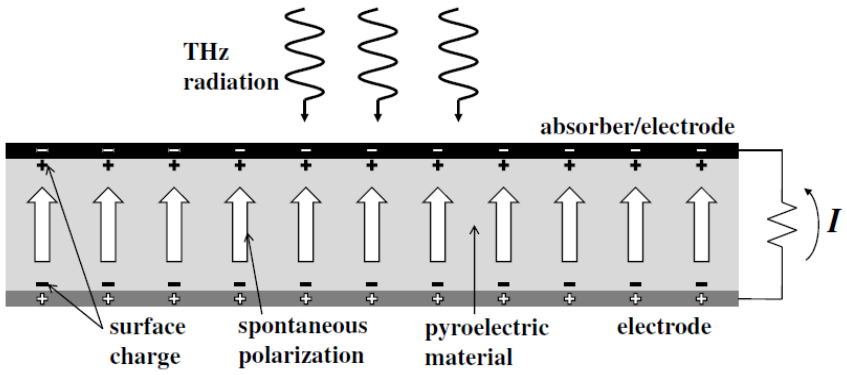

Figure 3.3.2 Schematic diagram of a typical pyroelectric detector. [20]

Figure 3.3.2 shows the scheme of a pyroelectric detector. The pyroelectric crystal cut perpendicular to its polar axis is sandwiched between two electrodes [99]. One side is usually treated to absorb incident radiation. The radiation generated heat raises the temperature of the pyroelectric crystal and induces a reduction of the spontaneous

polarization and the surface charge [20]. The attached electrodes on the crystal form a capacitor. If the circuit is closed, a current flows through it to compensate the change in the surface charge. A large load resistance is applied to achieve high responsivity and the signal is improved further by an operational amplifier. These detectors are used in AC mode due to the lack of pyroelectric current in steady state.

Golay-cell

Golay cells are sensitive pneumatic radiation detectors for the THz and the infrared ranges [100]. They are capable to sense THz radiation power levels down to the μW level [20]. Figure 3.3.3 shows the main components of a typical Golay cell. The modulated THz radiation passes through the front window then it is absorbed by an absorbing film.This energy induces thermal expansion of the gas enclosed in the pneumatic chamber and the resulting increase in the gas pressure deforms the flexible mirror attached to the backside of the chamber. The consequential path change of the reflected optical beam is sensed by the detection readout system.

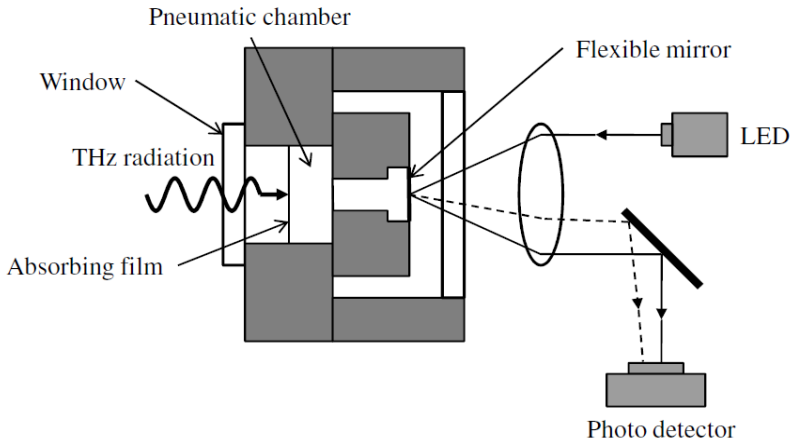

Figure 3.3.3 Schematic diagram of a Golay Cell. [20]

Golay cells are the most sensitive detectors among thermal radiation detectors at room temperature [20], but unfortunately have two major drawbacks: the relatively large detector size and the extreme sensitivity to mechanical (even acoustic) disturbances. Approximately half a century after their invention a new, micro-machined generation of small sized Golay cells has appeared on the market. Their detection schemes are based on either electric capacity variations [101] or tunneling displacement transducers [102].

THz cameras

Advanced manufacturing techniques has enabled the production of 2D-arrays of small sized micro-bolometers [103] and pyroelectric [104] detectors. Contrary to normal bolometers, micro-bolometers do not require cryogenic cooling at all, and have sensitivity that has reached the 100 pW/pixel level at 1 THz [105], making them more versatile and convenient instruments for THz imaging. They can be even used for spatially resolved broadband multi-channel spectrometry [106].

3.3.2. Time-domain spectroscopy of THz pulses

Techniques which generate broadband THz pulses to probe material properties and then measure their waveform after the interaction are known as THz time-domain spectroscopy [20]. Since a waveform contains complete information, a simple Fourier-transformation can retrieve both amplitude and phase of the spectral components. This allows simultaneous determination of the absorption and dispersion properties of a measured sample.

The static or low-frequency electric fields can induce a change in the refractive index of materials via the electro-optic effect [47]. In noncentrosymmetric crystal

structures the material's response is linearly proportional to the strength of the applied electric field, which is known as the Pockels effect. It can be described in a lossless medium as the $P_i^{(2)}$second-order polarization of matter by the $\chi_{ijk}^{(2)}$ second-order nonlinear susceptibility:

$$P_i^{(2)}(\omega) = 2\epsilon_0 \sum_{jk} \chi_{ijk}^{(2)} E_j(\omega) E_k(\omega_{THz}) \,. \qquad (3.3.1)\ [20]$$

Free space electro-optic (EO) sampling measures the electric field of broadband THz pulses in the time domain by utilizing the Pockels effect [20]. This technique is unique when compared to other traditional spectroscopic methods, as it is possible to directly measure the waveform of THz pulses as well as determine the amplitude and the phase of the measured field at the same time.

Figure 3.3.4 shows a typical setup of free-space EO sampling. In an ideal case, the optical group velocity and THz phase velocity are well matched inside the EO crystal, thus the optical pulse can experience the same section of the THz pulse as a constant electric field during co-propagation. By varying the relative timing between the two pulses, the entire THz waveform can be scanned. In the lower part of Figure 3.3.4, the evolution of the probe pulse polarization is shown with and without the THz field [20]. In the absence of a THz-field a linearly polarized optical pulse passes through the EO crystal without any alteration. Then the quarter wave plate transforms its polarization into circular. But in the presence of a THz-field the induced birefringence in the EO crystal changes the polarization rate of a linearly polarized optical probe pulse. Then the quarter-wave plate transforms its polarization into an almost, but not quite circular one. Finally, the Wollaston prism splits the probe beam into two orthogonal components, which are sent to a pair of balanced photo-detectors. This measures the intensity difference between the two orthogonal

components of the probe pulse, which is proportional to the applied THz field amplitude [20]. Too intense THz pulses can result in the induced birefringence being so strong that the polarization of the probe pulses are getting over-rotated hence the detected signal level is eventually decreasing.

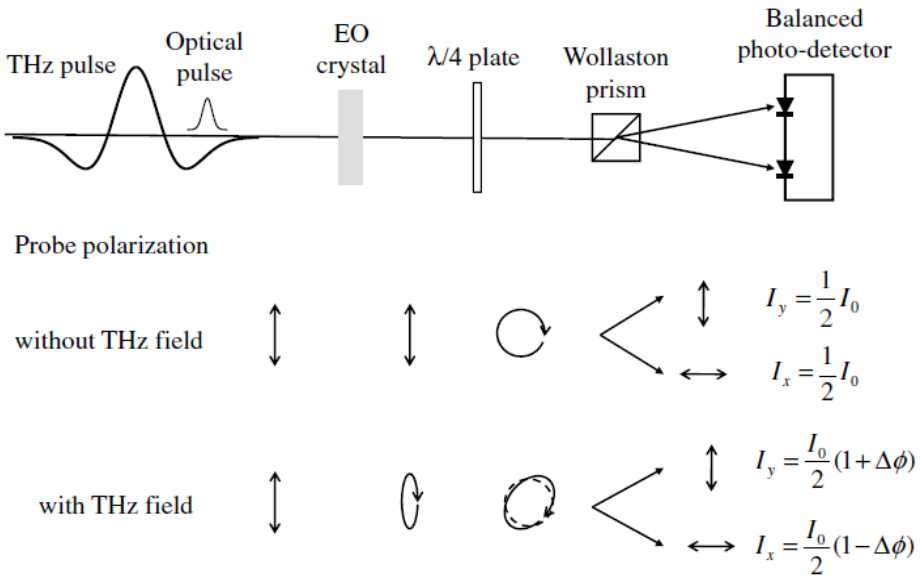

Figure 3.3.4 Schematic of a typical setup for free-space EO sampling. Probe polarizations with and without the THz field are shown before and after the polarization optics. [20]

EO sapling is a powerful technique but it has limitations on broadband THz pulse detection. The measured EO signal is the convolution of the THz electric field and the detector response function. A simple model can describe it as the product of three spectral filters acting on the complex amplitude spectrum of the THz pulse [107]. If the product of these filter functions has an uneven spectral response or insufficient bandwidth then the measured THz pulse waveform will be distorted and may significantly differ from the real one. Unfortunately, this spectral limitation is a realistic problem during experiments.

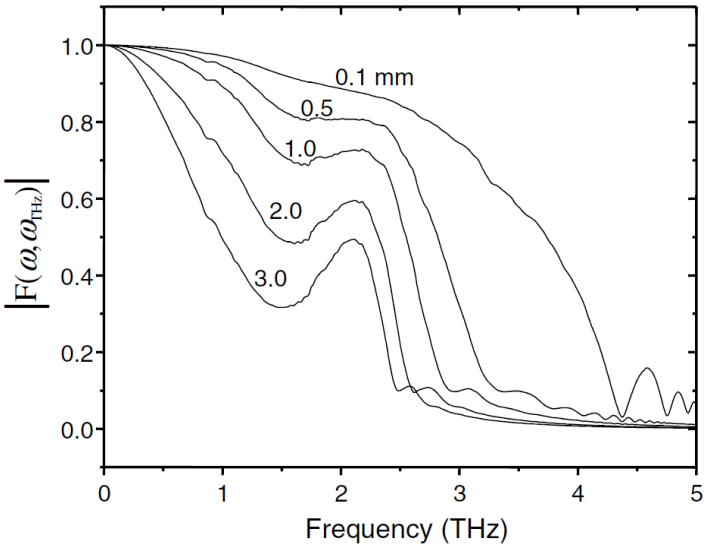

Figure 3.3.5 Normalized amplitude of the detector response function $F(\omega,\omega_{THz})$ for ZnTe. The lines are for the crystal thickness of 0.1, 0.5, 1.0, 2.0, and 3.0 mm when the 800nm optical pulse duration is 100 fs [20].

The first filter is related to the finite sampling pulse duration, the autocorrelation of the optical electric field:

$$C_{opt}(\omega_{\mathrm{THz}}) = \int_{-\infty}^{\infty} A_{opt}^{*}(\omega-\omega_0)A_{opt}(\omega-\omega_0-\omega_{\mathrm{THz}})d\omega. \qquad (3.3.2)\ [107]$$

This term has the smallest effect, as the filter spectrum is usually much broader than the spectrum of the measured THz pulse.

The second filter describes the frequency dependent EO susceptibility $\chi_{eff}^{(2)}$. It can strongly distort the measured EO signal and the corresponding spectrum especially around the phonon-resonance frequencies where $\chi_{eff}^{(2)}$ varies significantly [107]. The third filter describes the phase- mismatch between the optical probe pulse and the frequency components of the THz pulse. This also contains the THz absorption of the EO crystal and this effect can be reduced by a reduction in the thickness of the EO crystal.

Time-domain spectroscopy of broadband THz pulses is also possible by detecting the generated second-harmonic from gas plasma [44] or by measuring the induced photocurrent from photoconductive antennas [20] as it described earlier in Chapter 3.1.

4. Scientific goals

The importance of THz radiation has been significantly increased Over the recent decades due to the developing laser- and THz-science. The enhanced energy and spatiotemporal properties of the available THz sources has been already opened paths for several applications, but the source development is still a particularly active field. Just like any other source, OSCs are also suffer from different handicaps. The primary goal was to experimentally test alternative approaches which can solve their bottlenecks or exploit their unused capabilities. In this thesis, the generated THz and influenced IR radiation from DAST and DSTMS OSCs have been investigated and characterized in the following scenarios:

- **Unconventional pumping wavelengths:** The complexity and difficult accessibility of the usual high-energy pump sources around 1500 nm has resulted in the use of a common, Ti:sapphire pumping source around 800 nm. The results are compared with other THz sources pumped by this easily accessible pumping source. This is complemented with calculations about the expected THz spectrum close to the optimal pumping wavelength
- **Expanded crystal surface:** The comparison of a partitioned DSTMS, a mosaic set of smaller oriented crystals with a single crystal. This is inspired by the bottlenecks in production and manufacturing procedures of single crystals.
- **Recycling of pump beam:** The examination of the IR pump passed through a DAST crystal as a potential IR source with extreme spectral bandwidth.

5. Results

5.1. The pump source

During the experiments, different outputs of the same system were used as pump source. The system consists of two main units, a TW class Ti:sapphire laser system [108], and a commercial high-energy optical parametric amplifier (OPA).

The Ti:sapphire laser is a chirped pulse amplification system (Amplitude Technologies) consisting of an oscillator, a booster amplifier, a stretcher, a regenerative amplifier, two multipass amplifiers and a grating compressor. The system delivers pulses up to 20 mJ energy at 100 Hz repetition rate. It is capable to generate transform limited pulses with durations between 15 fs and 94 fs FWHM. The central wavelength is also tunable between 755 nm and 845 nm due to the built in acousto-optic programmable dispersive filter in the stretcher and the low-loss acousto-optic programmable gain control filter in the cavity of the regenerative amplifier [108]. During the experiments, the system was set to generate pulses with 50-60 fs duration at 800 nm central wavelength.

The high-energy OPA is a (custom) TOPAS-Prime from Light Conversion and it was pumped directly by the Ti:sapphire laser. The OPA consists of a white light generation stage as a broadband seed source, followed by three parametric amplifier stages using BBO as nonlinear medium. The accessible wavelength range is 1140-1600 nm with the signal and 1600-2600 nm with the idler beams. The system delivers pulses up to 3 mJ energy with 65 fs pulse duration at 1.5 μm wavelength, and it was used for the experiments with these settings.

5.2. THz generation with Ti:sapphire pumped DAST and DSTMS crystals

5.2.1. Introduction

OSCs are excellent THz emitters from several points of view. The very similar refractive index in the VIS/NIR and THz ranges makes it is possible to apply a simple collinear scheme for THz generation via optical rectification. Furthermore, their energy conversion efficiencies are higher than most of the currently known tabletop THz sources. They are usually pumped by a short pulsed (<100 fs) OPA in the NIR range around 1.5 µm wavelength. Unfortunately, OPAs are relatively expensive instruments and in most of the cases require a qualified person for the operation and daily fine-tuning.

The goal was to characterize OSCs pumped with a more easily, directly available pump sources, a turnkey system like Ti:sapphire lasers.

5.2.2. Experiment

The Ti:sapphire amplifier system was used for this studies with pulse energy about 10 mJ. The experimental setup is shown in Figure 5.2.1. The exposed organic crystals were a 0.86 mm thick DAST and a 0.2 mm thick DSTMS with 4.5 mm and 3 mm free apertures respectively. During the experiment, a 2 mm thick Teflon filter was used to reduce the residual pump background near to the detection level of the sensor.

The pulse energy of the generated THz was measured by a calibrated Golay cell. A conventional Michelson type interferometer was used to measure the first-order (field) autocorrelation of the THz pulses, with the same Golay cell as the detector. The THz

spectrum was obtained by Fourier transformation of the interferogram. This offers a more broadband frequency detection opportunity as compared to crystal based electro-optical sampling.

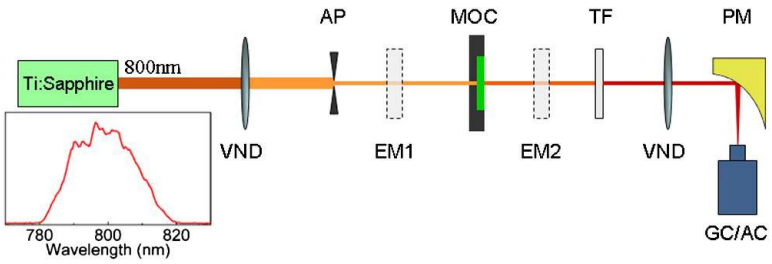

Figure 5.2.1 Schematic of the THz generation setup for organic crystals pumped at 800 nm with a Ti:sapphire amplifier (please see spectrum in the left bottom inset). VND: Variable neutral density filter wheel; AP: aperture; MOC: mounted organic crystal; TF: Teflon filter; PM: parabolic mirror; EM#: laser energy meter at two positions; GC: Golay-cell; AC: autocorrelator. [109]

The largest component of the nonlinear susceptibility tensor $\chi_{111}^{OR} = 490\ \mathrm{pm/V}$ [110] offers the most efficient THz generation within its phase matching range between 1.3 µm and 1.5 µm pump wavelengths. As predicted in Ref. [110] and experimentally confirmed in Ref. [111], another susceptibility tensor component $\chi_{122}^{OR} = 166\ \mathrm{pm/V}$ is the best suited for pump wavelengths between 680 and 800 nm. From an experimental point of view this means that the optical pump polarization must be aligned parallel to the crystallographic *b axis* and was done accordingly during the experiments.

5.2.3. Results

Figure 5.2.2 shows the generated THz pulse energy and the energy conversion efficiency as a function of the pump fluence for DAST and DSTMS crystals. The measured THz energy increases almost linearly with respect to the pump fluence up to 100 nJ for DAST (15.9 mm^2 emitter surface) and 50 nJ for DSTMS (7.1 mm^2 emitter surface) at 17 and 14 mJ/cm^2 pump fluencies, respectively. These energy values were measured behind a 2 mm thick Teflon

filter, and are not corrected with the ~25% average absorption across the 0.3–5 THz range. Up to this level, close to the damage threshold, no saturation could be observed in the THz energy. For 68 fs pulses (FWHM) at 800 nm, a damage threshold of ~300 GW/cm^2 (~20 mJ/cm^2) was measured for DAST and a slightly lower value was found for DSTMS.

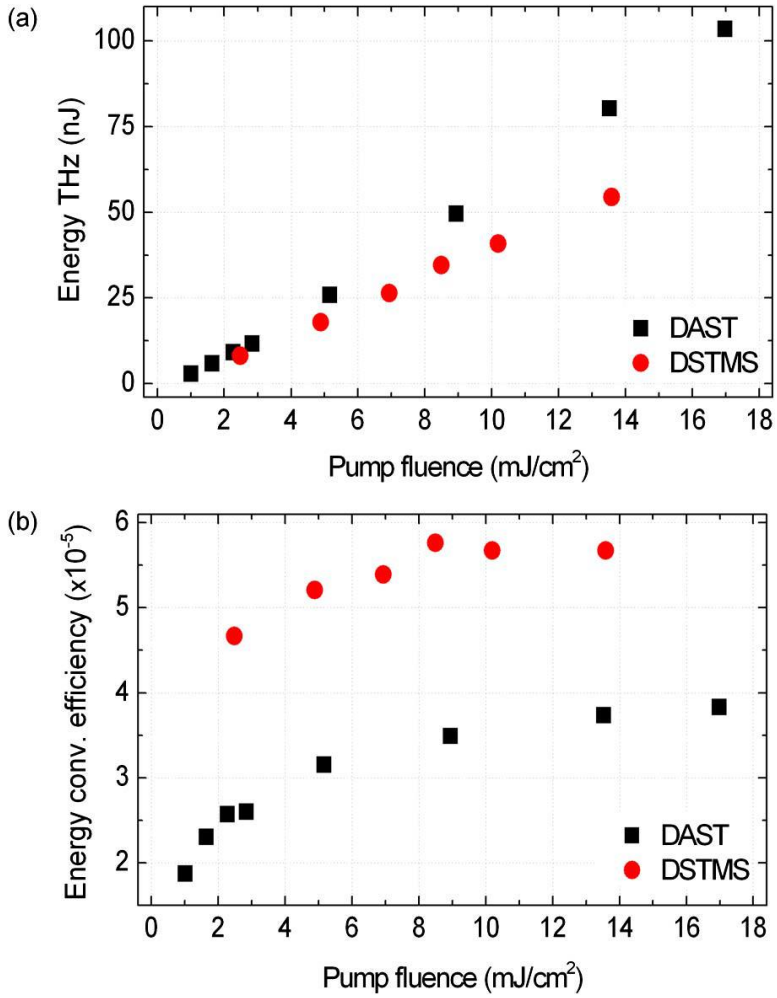

Figure 5.2.2 (a) THz pulse energy and (b) corresponding energy conversion efficiencies as functions of the applied Ti:sapphire pump fluence for DAST and DSTMS crystals, with emitting surfaces of 15.9 and 7.1 mm^2, respectively. Measured after a 2 mm thick Teflon plate. [109]

Figure 5.2.2(b) shows that the energy conversion efficiency slightly increases for higher pump fluence and levels of 6x10^{-5} for DSTMS and 4x10^{-5} for DAST, respectively. The conversion efficiencies stay 3 orders of magnitude lower than in the case of ~1.5 µm

pumping [79] and is presumed to be from the ~3 times lower nonlinear coefficient and the ~4 times shorter coherence length [96] [110],.

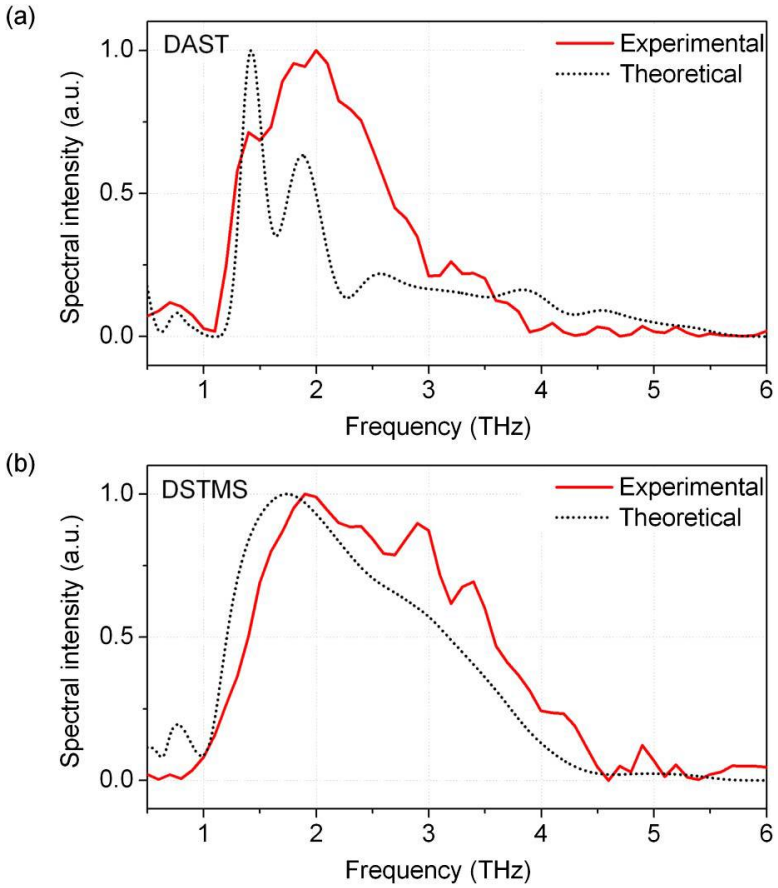

Figure 5.2.3 THz spectra for (a) DAST and (b) DSTMS pumped at 800 nm (fluence 6 mJ/cm^2) polarized along the b axis. The theoretical results already includes the filtering effect of the 2 mm thick Teflon sheet. [109]

Figure 5.2.3 shows the calculated theoretical the measured spectra of DAST and DSTMS. The measured spectra were obtained by Fourier transformation of the interferograms. The calculation **of theoretical curves** in Figure 5.2.3 and Figure 5.2.4 were carried out by Mojca Jazbinsek from the crystal manufacturer Rainbow Photonics AG (Switzerland). The model considered the crystal thickness, pulse duration, pump wavelength, velocity matching and linear THz absorption in the crystal [110]. These calculations neglects processes like nonlinear absorption of the pump and cascading, which can be significant especially in case of DAST [112] [113]. The theoretical curves

(dashed lines) in Figure 5.2.3 show an acceptable qualitative agreement with the experimental results. The spectra cover the ~1-5 THz range with a peak centered around 2 THz (DAST) and 2.5 THz (DSTMS). The components with lower frequencies than the phonon-active mode at 1.1 THz have just weak contributions to the overall spectrum.

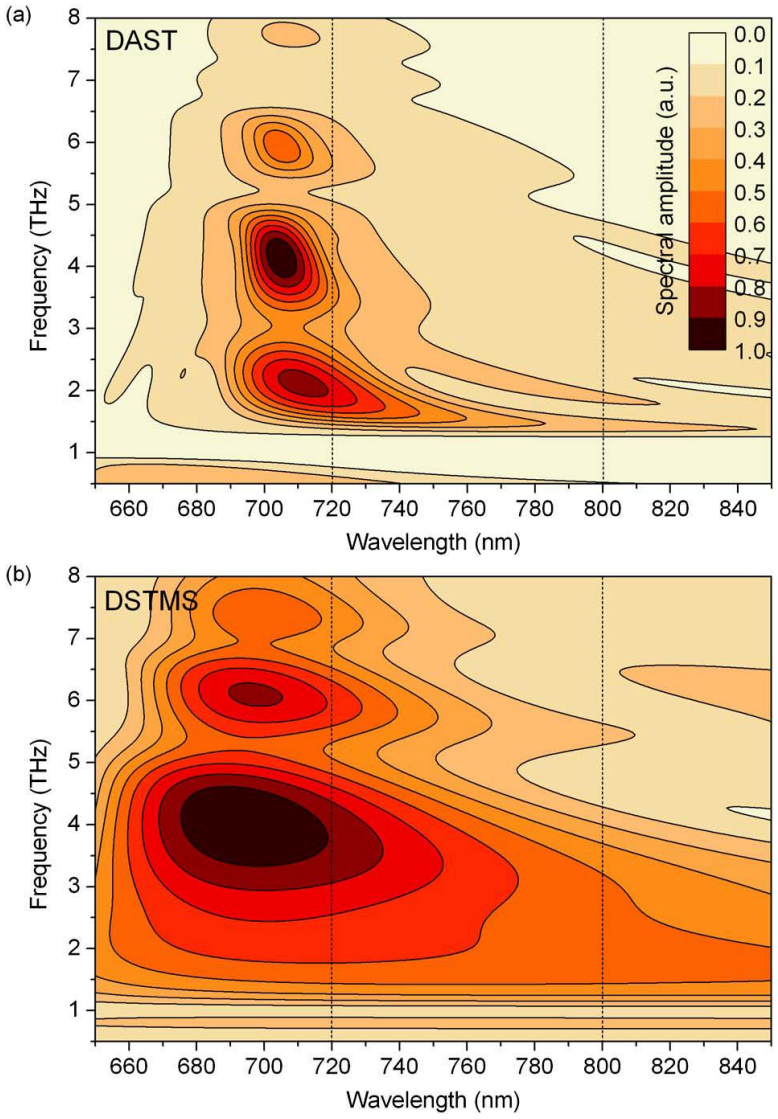

Figure 5.2.4 Calculated and normalized spectral amplitudes of the THz frequency components (same color scaling for (a) and (b)) as a function of the pump wavelength, in the case of (a) 0.86 mm thick DAST and (b) 0.2 mm thick DSTMS. The vertical dashed lines show the pump laser wavelengths used in the presented investigation. [109]

The maximum field strength can be estimated by the pulse energy and its spectral content. Assuming a diffraction limited spot size and Fourier limited pulse duration, a peak

electric field strength of 1 MV/cm can be calculated for DAST[3]. According to previous works [114] it is already sufficiently high to initiate nonlinear THz phenomena. The focusability of THz radiation from OSCs is excellent, because of the simple collinear generation scheme. The generated THz beam properties, such as almost distortion free pulse wave front and identical divergence for both lateral dimensions, help to achieve diffraction limited spot sizes [115].

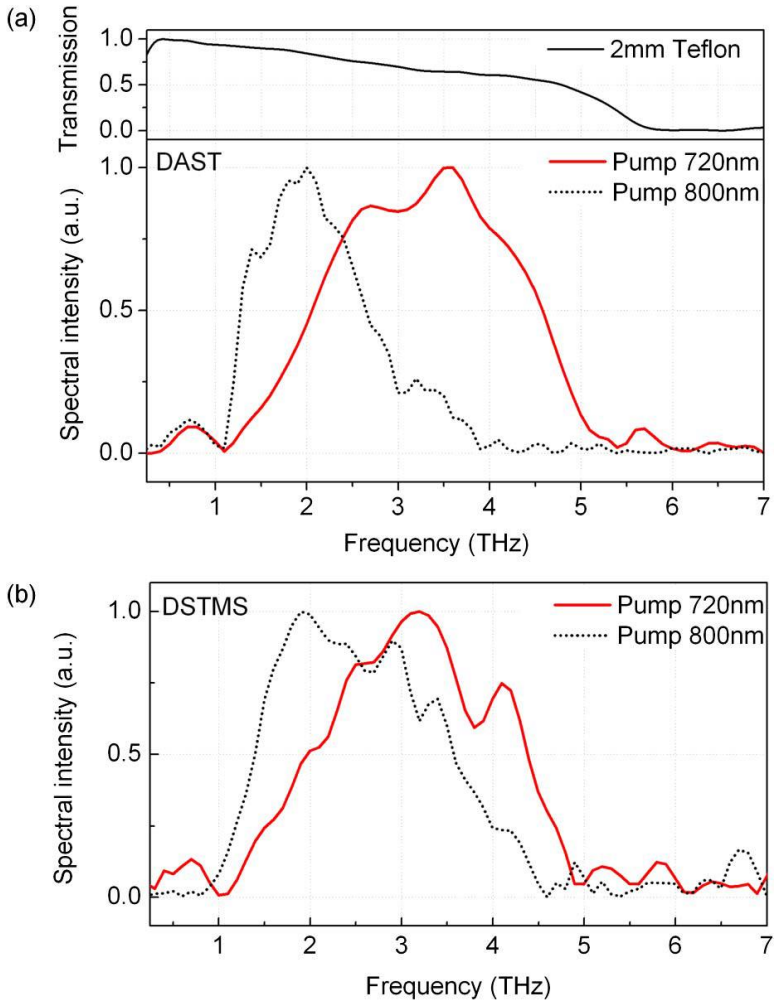

Figure 5.2.5 Measured THz spectra for (a) DAST and (b) DSTMS pumped at 720 and 800 nm. For visible pumping, the spectrum is limited by the Teflon transmission, cutting off for frequencies >5 THz, as shown in (a). [109]

[3] It was assumed that f=50 mm focusing optics with a numerical aperture of 1, 0.5 ps pulse duration, 2 THz central frequency and 0.1 µJ THz pulse energy.

The most effective visible pump wavelengths for broadband OR are located around 710 nm for DAST and 700 nm for DSTMS organic salt crystals, as it is shown by the calculations (Figure 5.2.4),. Unfortunately the typical wavelengths of a commercially available Ti:sapphire amplifier lies above these wavelengths. However, in order to verify the theoretical expectations, THz spectra of DAST and DSTMS organic salt crystals were recorded at 720 nm pump wavelength, using the frequency-doubled signal from an optical parametric amplifier. As predicted by the calculations (Figure 5.2.4), the velocity matching is also fulfilled under these conditions for higher THz frequencies, resulting in multi-octave spanning spectra covering the 0.5–5 THz frequency range (Figure 5.2.5).

5.2.4. Conclusions

The generation of high-energy THz pulses have been investigated in DAST and DSTMS OSCs pumped by a conventional Ti:sapphire laser. Broadband THz radiation has been demonstrated up to 5 THz with pulse energies up to 0.1 μJ after filtering out the residual IR pump. The major limitation of the maximal achievable THz pulse energy was the damage threshold of the OSCs. The possibility of generating higher THz frequencies was also demonstrated by using 720-nm pumping wavelength. The measured conversion efficiencies were comparable to other ordinary sources based on OR in crystals, like the semiconductor ZnTe (3.1×10^{-5}) [66]. Higher efficiencies could be expected for optimized crystal thickness. $LiNbO_3$-based sources show slightly better conversion efficiencies (1.16×10^{-4}) [116], but organic crystals allow accessing significantly higher frequencies well beyond 1 THz, and they work without pulse front tilting.

5.3. THz generation in a scalable partitioned DSTMS crystal

5.3.1. Introduction

Organic salt crystals have excellent energy conversion efficiency but the relatively low damage threshold and the small feasible crystal size due to production obstacles result in a strong limit on the available THz pulse energy and electric field strength.

Therefore, the goal was to overcome this bottleneck by using a partitioned crystal source. This will be characterized and compare its properties to those of a single crystal source.

5.3.2. Experiment

The OPA system(Chapter 5.1) was used to generate the pump pulses. The partitioned crystal surface (PCS) consisted of multiple parts of uncoated, small DSTMS crystals (Figure 5.3.1). These segments were glued together with transparent adhesive on a fused silica substrate, with a total surface of 400 mm^2. The substrate was antireflection coated for the pump and was oriented toward the OPA to avoid the THz absorption in the fused silica. The 5 mm thick host substrate transmitted more than 90% pump energy and introduces negligible group velocity dispersion at the pump wavelength. All DSTMS crystal segments were oriented to have their crystallographic axes parallel with each other in order to provide optimum phase-matching orientation across the entire PCS area. The individual organic crystal pieces were separated by about 200 µm and had a thickness of 500 ± 15 µm.

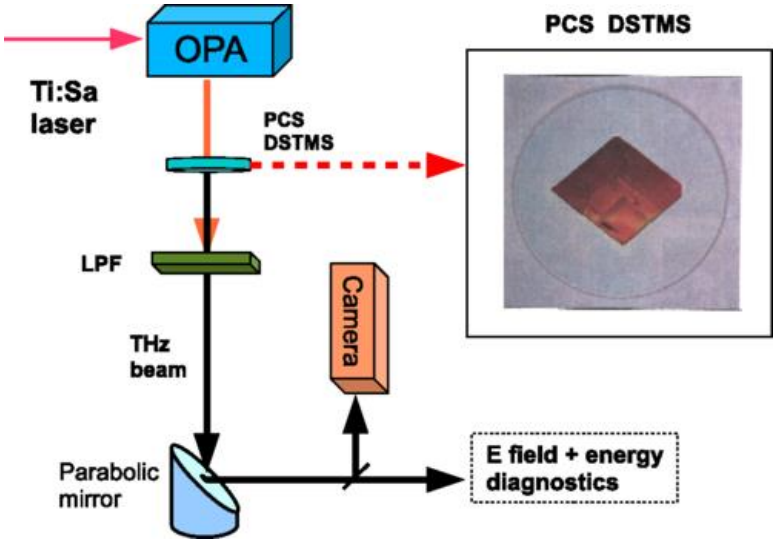

Figure 5.3.1 Tabletop terahertz source based on the partitioned DSTMS (PCS, shown in the inset). The crystal is pumped by an optical parametric amplifier (OPA). The THz beam is separated from the residual pump by a low-pass filter (LPF) and characterized by an electro-optical sampling, a THz camera, a Golay cell, and a THz autocorrelator. [95]

5.3.3. Results

The temporal and spectral shapes of the THz field from the PCS are shown in Figure 5.3.2.. The THz pulse reached electric peak field strengths of 0.6 GV/m and 2 T magnetic field strength with a near single-cycle waveform (Figure 5.3.2(a)), when pumped by the full mid-infrared energy available from the OPA. The temporal shape of THz field was measured in dry air using electro-optic sampling in 100 µm thick GaP crystal. The field strength was calculated from the THz spot size, pulse duration and energy. The multi-octave spanning THz spectrum (Figure 5.3.2(b)) peaks at 3.2 THz and covers frequencies up to 8 THz. It is free from periodic modulation which would indicate a significant temporal/phase shift between the beamlets. The dips at around 1 THz and 5 THz are due to absorption caused by phonon active modes in the organic crystal [117]. The emission properties of the PCS are compared, at identical pump fluence, to a singlet small-size DSTMS crystal (3×3 mm^2) of same thickness. The comparison reveals similar field and spectral shapes in the focus

but 3 times larger field strength for the PCS. This gives a first indication that the THz field characteristics are neither spoiled by discontinuities in the PCS emitter nor by negative interference of fields emitted from different crystal parts.

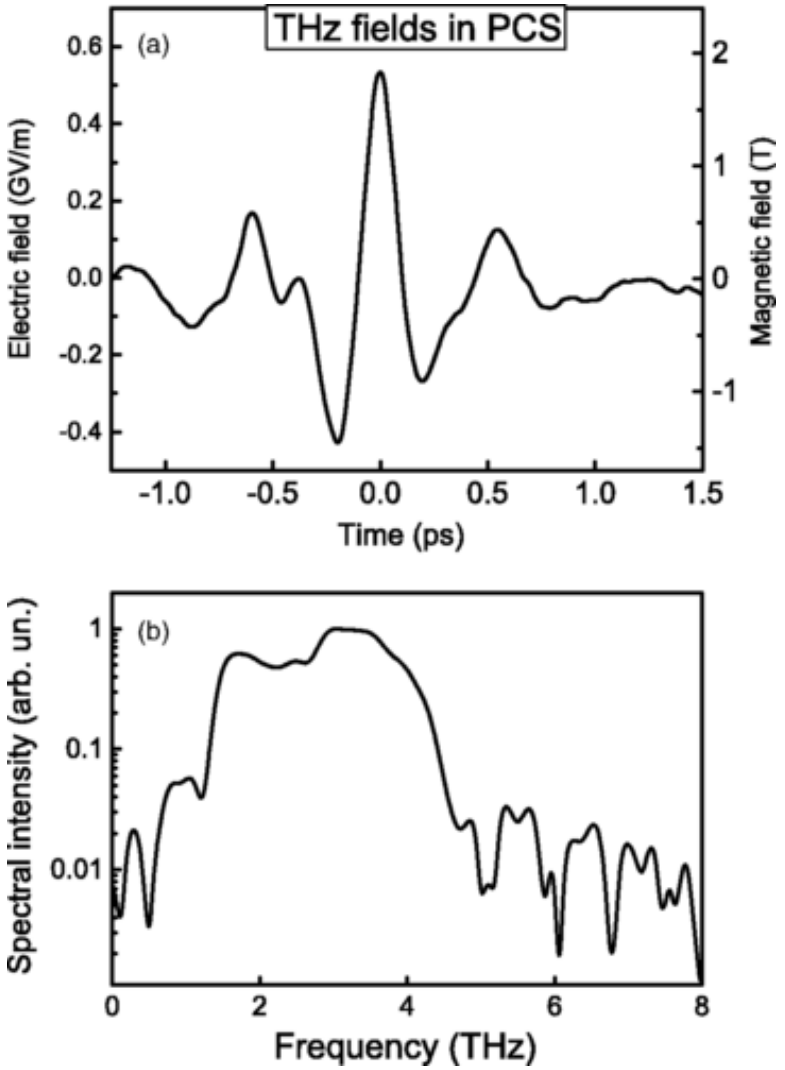

Figure 5.3.2 The electric field (a) and the corresponding spectrum (b) of the THz pulses obtained by optical rectification in a partitioned DSTMS crystal structure. [95]

In principle tight focusing could be limited by wavefront aberrations caused by discontinuities and by errors in orientations and thickness of the individual PCS. In order to verify the influence of these effects on beam quality, the THz beam distortions were characterized by recording the intensity profile of the beam in the near field and the far field. The near-field profile (Figure 5.3.3(a)) was recorded by imaging the PCS onto an

uncooled microbolometer THz imager (NEC Corporation, IRV-T0830, 23.5 μm pixel pitch). The gaps between the three crystal segments were clearly observable. The sum-area of the "shadow zones" (Figure 5.3.3(c)) with intensities less than 25% is approximately 15% of the full pumped area. The additional intensity variation across the emitting area originates from the non-uniformities of the pump beam. The emitted THz radiation from the PCS consisted of three collinearly propagating beamlets in the near-field. These beams were also measured at the focus point of an off-axis parabolic mirror with a numerical aperture of 0.25 and focus of 100 mm. At the focal plane, the three beamlets combined perfectly into a single spot with smooth intensity distribution as shown in Figure 5.3.3(b). The corresponding circular THz spot size was measured to be 270 μm (FWHM), which is close to the diffraction limit. Although the M^2 number is suited for monochromatic beams based on several measurements along its propagation axis, an approximate value of $M^2 \approx 1.8$ can be calculated for the broadband THz focal spot.

The experimental results were reproduced by modeling in ZEMAX optical design code (insets in Figure 5.3.3(a) and Figure 5.3.3(b)). The modelling was done by Carlo Vicario from Paul Scherrer Institute (Switzerland). Both experimental and numerical results reveal that the discontinuities present in the PCS play a negligible role on the THz beam focusing properties. The THz intensity distribution at the focus is not significantly influenced by the diffraction from the emitter gap nor the non-uniform pump beam. The constructive interference among the contributions from the different crystal segments resulted in an extremely strong electric field (Figure 5.3.2) in the focal region.

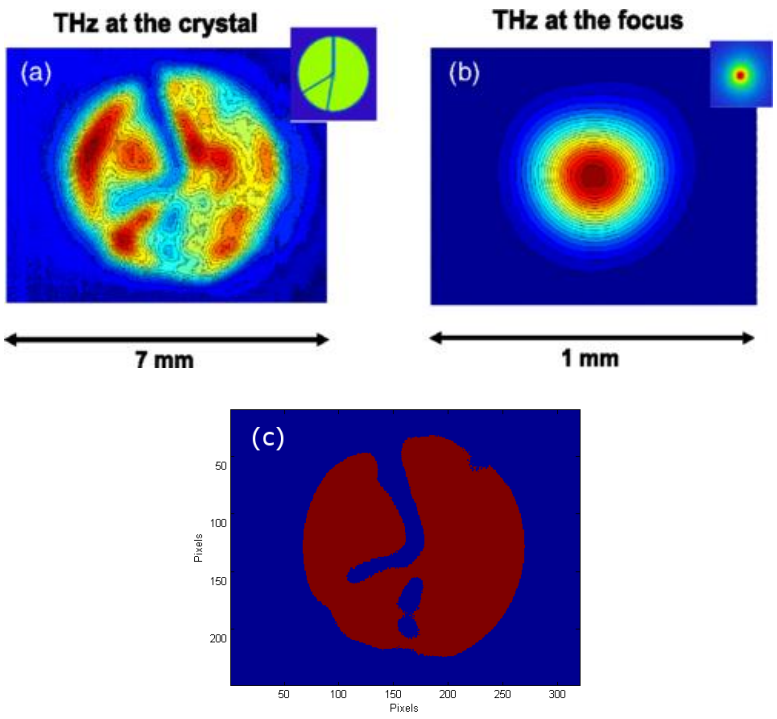

Figure 5.3.3 Measured THz beam profile at (a) the crystal output and at (b) the focus of parabolic mirror with numerical aperture of 0.25. (c) highlights the shadow zones inside of the beam with intensities less than 25% originated from the gaps among crystal segments. The insets show the (a) structure of the mosaic DSTMS crystal and (b) the simulated intensity profile at the focus of parabolic mirror. [95]

Figure 5.3.4 shows the measured Gouy phase shift along the focal region ($|z|<1.5z_{Rayleigh}$), where the individual beamlets formed a single-beam like unity. A clear polarity reversal of the field due to the Gouy phase shift was observed (Figure 5.3.4 insets) [118] [119], whereas other features of the waveform were not altered. The corresponding Gouy phase shift (black symbols) agrees with theoretical expectations (fit). The measured phase values were retrieved from the Fourier transformed of different waveform measurements via electro-optic sampling, where the sampling crystal was placed around the focal point at various positions along the beam propagation axis.

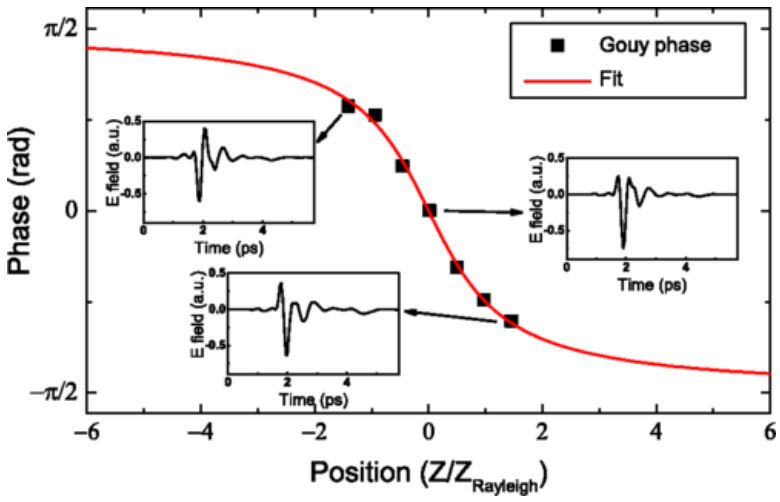

Figure 5.3.4 Measured Gouy phase shift (dots) and polarity reversal of the net electric field (insets) across the focus, measured by electro-optic sampling. [95]

A single organic DSTMS crystal offers conversion efficiency around 1% [117] and a similar value is expected for PCS. Figure 5.3.5 illustrates the measured THz pulse energy density (fluence) and the energy conversion efficiency of PCS as a function of the pump fluence. The THz pulse energy density was almost linearly scaled with larger pump fluence (Figure 5.3.5(a)) and reached a peak value of 170 μJ/cm^2 at 18 mJ/cm^2, close to the damage threshold of the crystal (>20 mJ/cm^2). The pump-to-THz energy conversion efficiency (Figure 5.3.5(b)) shows a linear increase up to 1.1% at 7 mJ/cm^2 pump, before saturation effects take place. For the PCS (black squares) the THz yield was slightly lower (on average 15% less) compared to the single, small-size crystal (red circles) due to the loss and scattering occurred at the gaps and the loss of pump power at the substrate interfaces. Using the full area of the PCS with the maximum pump fluence would result in ≈0.68 mJ THz pulse energy.

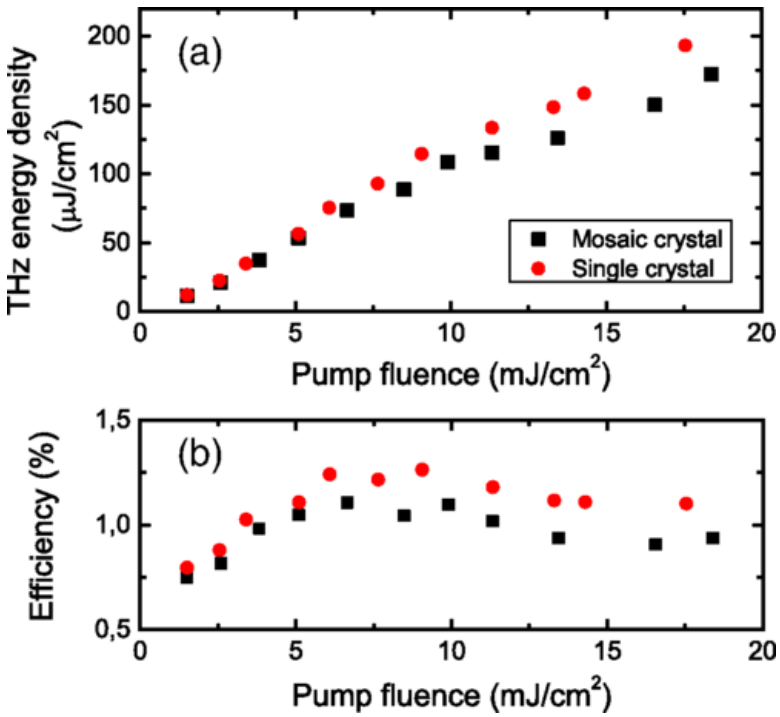

Figure 5.3.5 (a) THz pulse energy density for PCS DSTMS nonlinear crystal (black dots). The THz energy density almost linearly increases for larger pump fluence, up to pump fluence close to the damage threshold of the crystal (>20 mJ/cm^2). The characteristics are similar to the small-size single crystal (red circles). (b) Corresponding conversion efficiency in dependence of the pump fluence. The THz pulse energy has been recorded by means of a calibrated Golay cell. [95]

The actual energy conversion efficiency was even higher considering that almost 70% of input pump energy was absorbed during propagation through the crystal. Thus on average, only ~55% of the OPA energy contributed effectively to THz generation. The observed high efficiency was due to cascading OR. During this process, a pump photon emits one THz photon and undergoes a small redshift and then contributes again to THz generation by OR. This cascaded $\chi^{(2)}$ nonlinearity results the entire pump spectrum undergoes shifts towards longer wavelengths. After a sufficient amount of THz generation, SFG between pump and THz causes noticeable pump spectral broadening in the short wavelength side. These effects depend strongly on the pump fluence, shown in Figure 5.3.6(a). The pump peak wavelength is shifted by more than 40 nm from 1460 nm (205 THz) to 1500 nm (200 THz) for an increase in pump fluence Figure 5.3.6(b). Similar,

but less pronounced red-shifting has been reported for other OR crystals over long interaction lengths [120]. In this experiment cascading OR leaded to a much higher THz conversion efficiency than theoretical predicted by the Manley-Rowe limit: $N(h\nu_{THz}) \leq N(h\nu_p)$. $N(h\nu_{THz})/N(h\nu_p) \approx 1.4$ has been calculated for the spectral center frequency of 2.9 THz considering the pump absorption.

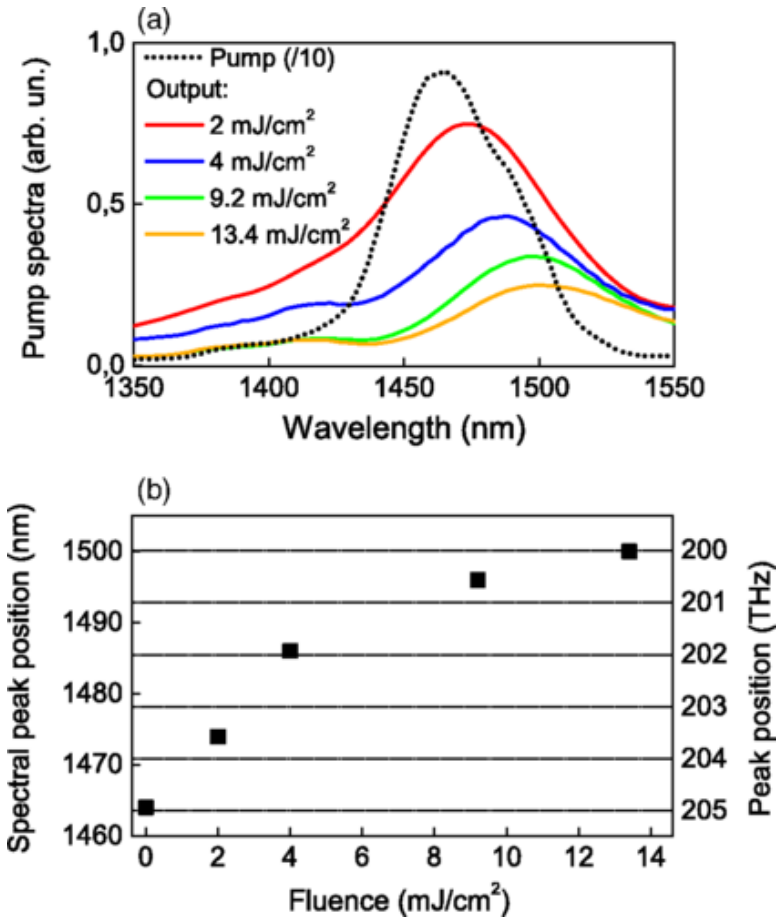

Figure 5.3.6 (a) Pump spectra and (b) corresponding spectral peak redshift caused by cascaded optical rectification in the organic crystal [95].

5.3.1. Conclusions

The experiments proved the concept of large, partitioned THz emitter. The introduced technique is a feasible way to scaling up the THz field strength and energy of a compact

THz source. Despite of the discontinuities in the PCS, nearly diffraction limited focus spot size could be achieved, and distortions in the beam were not observable around its focal plane. The DSTMS-based PCS just like single crystals provides a high laser to THz energy conversion efficiency of ≈1%, due to cascading optical rectification which exceeds the Manley-Rowe limit even over a short interaction length of ~500 μm. The PCS provided on average only 15% less emitted THz energy density than a single crystal. The constructive interference of individual beamlets in the focus resulted in a single-cycle, linearly polarized THz transient with 0.6 GV/m electric and 2 T magnetic peak field strengths in the 1–8 THz frequency range. The demonstrated constructive interference is fundamental to reach the higher THz field strengths and proves that the power of the PCS approach for up-scaling the THz pulse energy while keeping the excellent spatiotemporal beam properties in the focus. Further up-scaling in field is only limited by the available pump laser energy as the partitioned organic crystal structure can easily be expanded in size.

5.4. Spectral broadening of intense infrared pulses in DAST crystal

5.4.1. Introduction

The uniquely large nonlinear coefficient of DAST is advantageous for THz generation and also for other nonlinear processes. Large spectral broadening has been demonstrated in phase-mismatched SHG in materials with large second order susceptibility [121] [122]. Energetic ultrabroad broadband pulses in the near and mid-infrared region are interesting for several applications like high harmonic generation [123] or hyperspectral imaging in medicine [124].

The goal was to characterize this exceptional spectral broadening and gather information for possible future applications.

5.4.2. Experiment

The experimental setup is shown in Figure 5.4.1. A 200 µm thick DAST crystal with an aperture of 5 mm was illuminated by a collimated, laser beam at 1.5 µm from the OPA. The *α*-axis of the DAST crystal was oriented parallel to the pump polarization to maximize spectral broadening. In this way the advantage of the largest nonlinear coefficient: d_{111}=290 pm/V could be taken, which is also the typical crystal orientation for efficient THz generation by optical rectification.

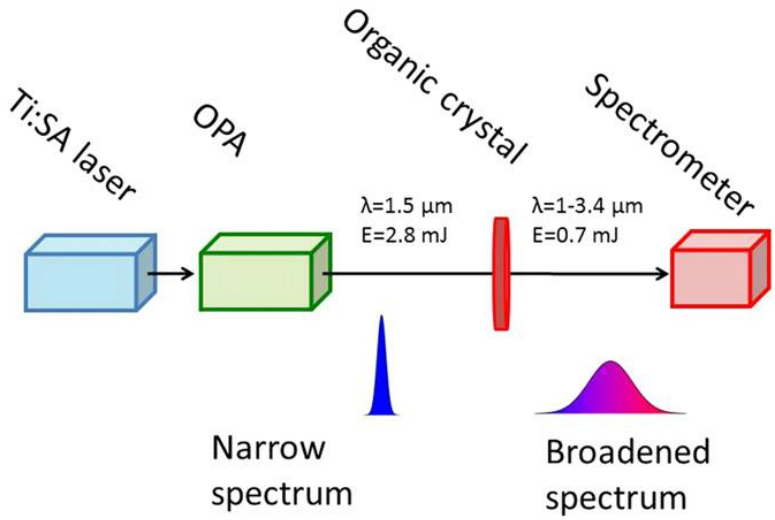

Figure 5.4.1 The experimental setup: An optical parametric amplifier (OPA) pumped by a multi-mJ femtosecond Ti:Sa initiates the spectral broadening in DAST. The multi-octave IR spectrum is measured with a scanning near infrared spectrometer. [113]

The spectrum generated in DAST is measured using a near-infrared spectrum analyzer based on a tunable acousto-optic bandpass filter [125]. The acousto-optic interaction takes place in a 25 mm long TeO_2 crystal. Scanning the frequency of a monochromatic acoustic wave allows selection of a narrow optical spectral line. A Peltier-cooled HgCdTe detector records the intensity of the diffracted optical beam at maximum repetition rate of 100 Hz. The overall spectral intensity is then reconstructed by post-processing based on integration and normalization. The spectrometer's sensitivity covers the 1-5 μm wavelength range with resolution better than 5 cm^{-1} and a dynamic range larger than 40 dB. In the experiment, the beam was focused at the spectrometer entrance slit with a typical fluence of 60–130 $\mu J/cm^2$. Unfortunately the proper single-shot temporal characterization of the extremely broad IR spectrum generated in the experiment was unfeasible with the available instrumentation [126].

5.4.3. Results

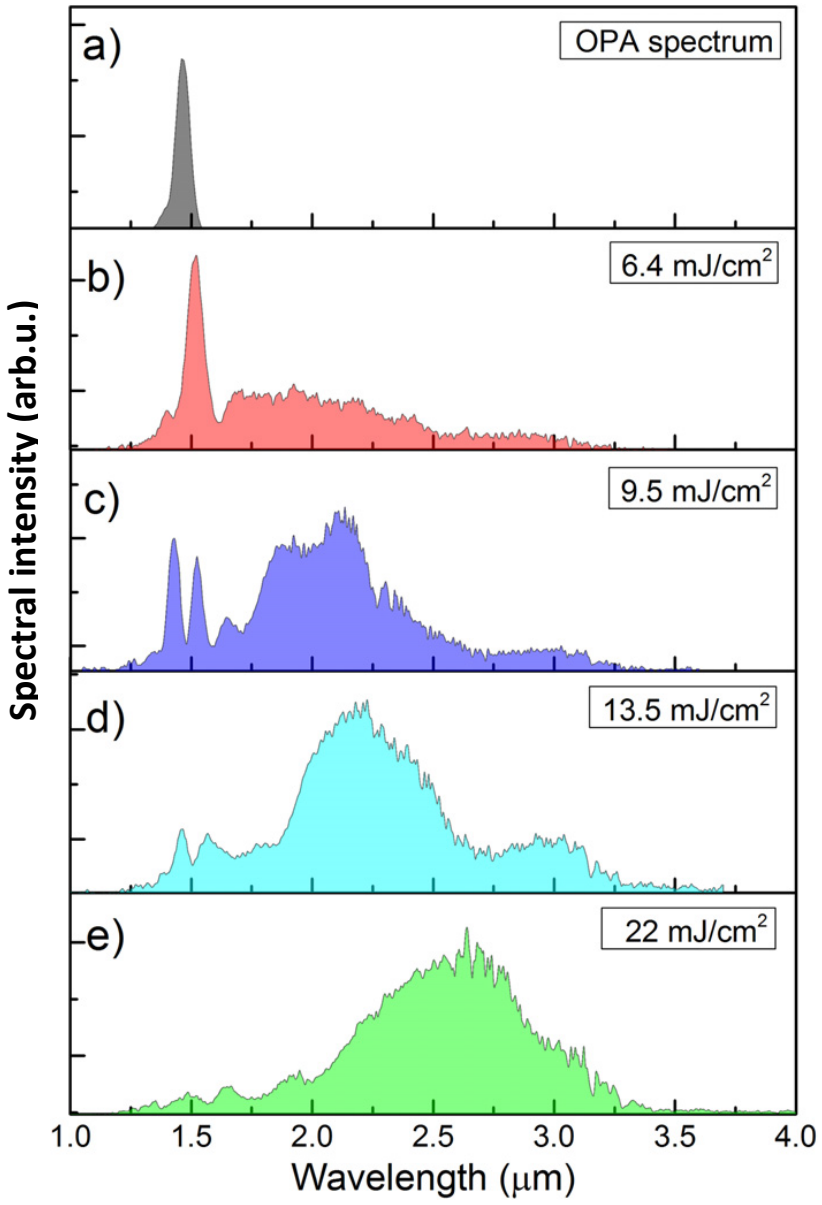

Figure 5.4.2 Experimental results on spectral broadening in 200 μm DAST for different values of the peak fluence. As illustrated the original spectrum of the OPA (a) is progressively broadened and redshifted towards SWIR (b)–(e). The spectral intensity is shown on a linear scale. [113]

Figure 5.4.2 shows the spectra generated in the DAST crystal pumped with different peak fluences. The original OPA spectrum shown in gray (Figure 5.4.2(a)) was 80 nm wide at FWHM and centered at 1500 nm. An increase in pump intensity resulted in the broadening spectrum is progressively broadened and a shift towards longer wavelengths.

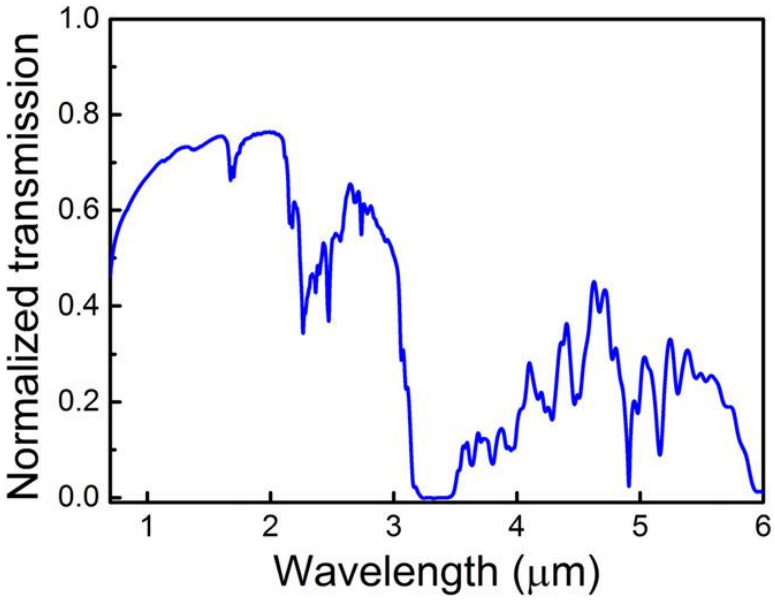

Figure 5.4.3 Linear unpolarized spectral transmission of a 200 μm thick DAST sample measured by Fourier transform spectroscopy. The curve has not been corrected for the Fresnel losses at the input and output surfaces, which are approximately 13% per surface for the DAST refractive index of 2.1. [113]

From 6.4 mJ/cm^2 pump fluence, a tail extending towards the long wavelengths beyond 3 μm was visible besides the original spectrum (Figure 5.4.2(b)). At higher pump fluence, more energy was converted from the pump to near-infrared frequencies (Figure 5.4.2(c)–(d)). At the highest pump fluence of 22 mJ/cm^2 (green curve), close to the optical damage threshold of DAST, the pump was completely converted to a supercontinuum with central wavelength of 2.6 μm (Figure 5.4.2(e)). At this fluence the output spectrum covered a continuous range from 1.2 to 3.4 μm, which corresponds to about 1.5 octaves. The low frequency cut-off can be attributed to the strong linear absorption in DAST. Figure 5.4.3 shows the linear transmission spectrum of the 200 μm DAST sample. There are two distinct cascaded $\chi^{(2)}$-processes which could directly contribute to the spectral broadening: the phase mismatched SHG [121] and electro-optical modulation driven by OR generated THz pulses [127]. Phase mismatched SHG can give rise to strong broadening in a process similar to Kerr-like nonlinearity, with negative sign (self-defocusing) when $\Delta k > 0$. Such a fast

nonlinearity typically generates a symmetrically broadened spectrum. The optical rectification in DAST produces an intense THz pulse, which co-propagates with the incoming optical beam and modulates the index of refraction by the electro−optical effect [128]. A nonlinear refraction process with delayed response, such as Raman scattering or thermal effects, could also contribute to asymmetric spectral broadening and red-shift.

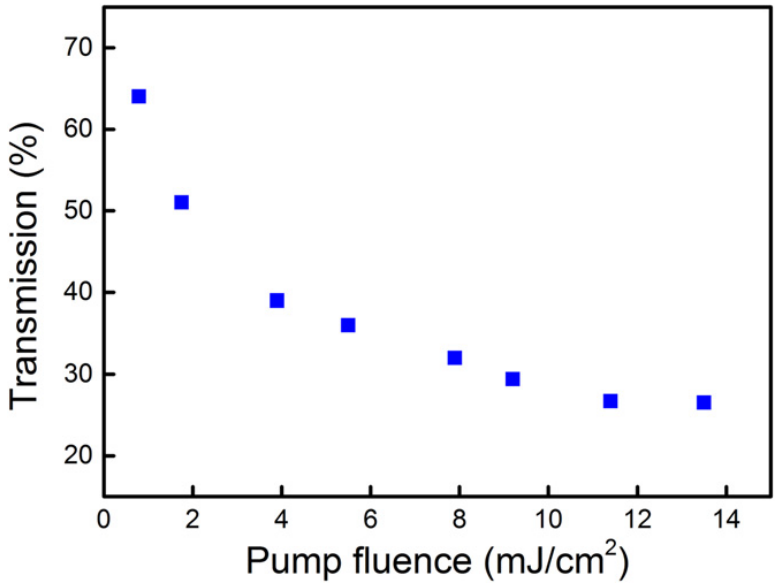

Figure 5.4.4 Total transmission in DAST pumped at 1500 nm, including the Fresnel losses, as function of the peak input fluence. [113]

Another interesting feature is the nonlinear transmission as function of the pump fluence shown in Figure 5.4.4. At low input fluences the transmission (not corrected for Fresnel losses), was as high as 73%, while as increase in the pump fluence cause a rapid drop to less than 40% and saturated at just below 30% for pump fluence larger than 10 mJ/cm^2. Such a high level of absorption may raise the problem of different thermal effects. Unfortunately, the thermal properties of DAST are not investigated, but based on the multiple strong phonon resonances of the crystal structure [91], one can assume a fairly high level of thermal conductivity. That could reduce the thermal gradient in pumped crystals therefore phenomena like thermal lensing caused phase front distortions probably

plays negligible role in most of the cases e.g. THz generation. In case of the broadband IR pulses it could affect the shortest achievable pulse duration and make pulse compression more challenging.

5.4.4. Conclusions

Unprecedented spectral broadening was observed in DAST presumably caused by multiple nonlinear processes such as cascaded $\chi^{(2)}$ processes, Raman scattering and thermal effects. A spectrum spanning over 1.5-octave between 1.2 µm and 3.5 µm was achieved for pump fluences larger than 10 mJ/cm^2. The crystal provided pulse energies up to 700 µJ with conversion efficiency of 25% or better. Scaling the pulse energy up to several mJ is feasible with a larger DAST crystal and higher pump energy while keeping its fluence constant.

5.5. Thesis statements

1) It has been demonstrated that the conversion efficiency of DAST ($4x10^{-5}$) and DSTMS ($6x10^{-5}$) organic salt crystals are comparable to other optical rectification based THz sources such as ZnTe ($3.1x10^{-5}$) or $LiNbO_3$ ($11.6x10^{-5}$) crystals when pumped at Ti:sapphire wavelengths. [109]
2) It was shown that the spectra of the generated THz radiation extends towards the higher frequencies when the DAST or DSTMS organic salt crystals were pumped around the optimal 680-740 nm wavelengths instead of Ti:sapphire wavelengths. This is due to the spectrally broader phase-matching properties. [109]
3) It was experimentally proved that individual THz beamlets from a partitioned crystal, a mosaic arrangement of smaller oriented crystal segments, are capable of a high level of constructive interference, which was manifested in a near single-cycle THz pulse waveform and a Gaussian like smooth focal spot with beam quality factor of $M^2 \approx 1.8$. A THz beam generated in a partitioned crystal and a THz beam generated in a single crystal have technically identical spatio-temporal beam quality around their focal planes. [95]
4) It was experimentally shown that the passing infrared pump beam in a DAST organic salt crystal can undergo extreme spectral broadening and achieve ~1.5-octave broad spectrum covering the range between 1.2 μm and 3.5 μm. [113]

5.6. Tézispontok

1) Demonstráltuk, hogy a DAST ($4x10^{-5}$) és DSTMS ($6x10^{-5}$) organikus sókristályok hatásfoka összemérhető más, optikai egyenirányításon alapuló THz-es forrásokéval, mint a ZnTe ($3.1x10^{-5}$) vagy a $LiNbO_3$ ($11.6x10^{-5}$) kristályok, amikor a Titán-zafír lézerek hullámhosszán vannak pumpálva. [109]
2) Megmutattuk, hogy a keltett THz-es sugárzás spektruma kibővült a magasabb THz-es frekvenciák felé, amikor a DAST vagy DSTMS organikus sókristályok az optimális 680-740 nm körüli hullámhosszokkal voltak pumpálva a Titán-zafír lézerek hullámhossza helyett, köszönhetően a spektrálisan szélesebb fázisillesztési tulajdonságaiknak. [109]
3) Kísérleti úton bizonyítottuk, hogy egy osztott struktúrájú kristály (kisebb orientált kristály szegmensek mozaik elrendezésben) esetén, a belőle származó különálló nyalábok képesek a magas-fokú koherens interferenciára, amely a közel egyciklusú THz-es impulzus hullámformájában valamint az $M^2 \approx 1.8$ értékű nyaláb faktorral rendelkező Gauss-szerű látható torzulásoktól mentes fókusz foltban nyilvánul meg. Ezért egy osztott struktúrájú kristályban keltett THz-es nyaláb és egy egykristályban keltett THz-es nyaláb tér és időbeli tulajdonságai technikailag azonosak a fókuszpontok közelében. [95]
4) Kísérletileg megmutattuk, hogy a DAST organikus sókristályon áthaladó pumpáló infravörös nyaláb extrém mértékű spektrális kiszélesedésen mehet keresztül és elérheti a ~1.5-oktávos spektrális sávszélességet lefedve ezzel az 1.2 µm és 3.5 µm között tartományt. [113]

6. Publication list / Publikációs jegyzék

1. Publications in the topic of thesis / Az eljárás témakörében készült publikációk

B. Monoszlai, C. Vicario, M. Jazbinsek, C.P. Hauri: “High energy terahertz pulses from organic crystals: DAST and DSTMS pumped at Ti:sapphire wavelength”, *Optics Letters, Vol. 38, Issue 23, pp. 5106-5109 (2013)*

Carlo Vicario, **B. Monoszlai**, and Christoph P. Hauri: “GV/m Single-Cycle Terahertz Fields from a Laser-Driven Large-Size Partitioned Organic Crystal”, *Phys. Rev. Lett. 112, 213901, (2014)*

C. Vicario, **B. Monoszlai**, G. Arisholm, and C.P. Hauri: “Generation of 1.5-octave intense infrared pulses by nonlinear interactions in DAST crystal”, *Journal of Optics, Vol. 17, 094005, (2015)*

2. Non-refereed conference abstracts in the topic of thesis / Az eljárás témakörében készült nem referált konferencia absztraktok

-

3. Publications in other topics / Az eljárás témakörén kívül készült publikációk

C. Vicario, **B. Monoszlai**, Cs. Lombosi, A. Mareczko, A. Courjaud, J. A. Fülöp, C. P. Hauri: “Pump pulse width and temperature effects in lithium niobate for efficient THz generation”, *Optics Letters, Vol. 38, Issue 24, pp. 5373-5376 (2013)*

P. N. Juranic, A. Stepanov, P. Peier, C. P. Hauri, R. Ischebeck, V. Schlott, M. Radovic, C. Erny, F. Ardana-Lamas, **B. Monoszlai**, I. Gorgisyan, L. Patthey, R. Abela: “A scheme for a shot-to-shot, femtosecond-resolved pulse length and arrival time measurement of free electron laser x-ray pulses that overcomes the time jitter problem between the FEL and the laser”, *JINST, Vol. 9, pp. P03006 (2014)*

A. Trisorio and M. Divall and **B. Monoszlai** and C. Vicario and C. P. Hauri: “Intense sub-two-cycle infrared pulse generation via phase-mismatched cascaded nonlinear interaction in DAST crystal”, *Optics Letters, Vol. 39, Issue 9, pp. 2660-2663 (2014)*

P. N. Juranić, A. Stepanov, R. Ischebeck, V. Schlott, C. Pradervand, L. Patthey, M. Radović, I. Gorgisyan, L. Rivkin, C. P. Hauri, **B. Monoszlai**, R. Ivanov, P. Peier, J. Liu, T. Togashi, S. Owada, K. Ogawa, T. Katayama, M. Yabashi, and R. Abela: “High-precision x-ray FEL pulse arrival time measurements at SACLA by a THz streak camera with Xe clusters”, *Optics Express, Vol. 22, Issue 24, pp. 30004-30012 (2014)*

C. Vicario**, B. Monoszlai**, M. Jazbinsek, S.-H. Lee, O-P. Kwon and C. P. Hauri: “Intense, carrier frequency and bandwidth tunable quasi single-cycle pulses from an organic emitter covering the Terahertz frequency gap”, *Scientific Reports 5, Article number: 14394 (2015)*

J. A. Fülöp, Gy. Polónyi, **B. Monoszlai**, G. Andriukaitis, T. Balciunas, A. Pugzlys, G. Arthur, A. Baltuska, and J. Hebling: “Highly efficient scalable monolithic semiconductor terahertz pulse source”, Optica Vol. 3, Issue 10, pp. 1075-1078 (2016)

Gy. Polónyi, **B. Monoszlai**, G. Gäumann, E. J. Rohwer, G. Andriukaitis, T. Balciunas, A. Pugzlys, A. Baltuska, T. Feurer, J. Hebling, and J. A. Fülöp: “High-energy terahertz pulses from semiconductors pumped beyond the three-photon absorption edge”, Optics Express Vol. 24, Issue 21, pp. 23872-23882 (2016)

4. Non-refereed conference abstracts in other topics / Az eljárás témakörén kívül készült nem referált konferencia absztraktok

-

7. Acknowledgements / Köszönetnyilvánítás

Firstly, I would like to thank my supervisor, Dr. József András Fülöp for his guidance and the several opportunities what he provided including involving me in the lab work from the end of my BSc studies. I am especially grateful for his support for the SCIEX scholarship, which allowed me to spend more than a year at the Paul Scherrer Institute (PSI) in Switzerland, where I could test myself in an international environment and build new relationships.

I would like to thank Prof. Dr. Christopher Hauri from PSI for his hospitality, for receiving me into his group, as well as for his guidance and his experimental ideas. I would also like to thank Dr. Carlo Vicario for his guidance and help in the lab especially with the laser system and for his introduction into the world of organic crystals. I also thank Mojca Jazbinsek from Rainbow Photonics

Először is szeretném megköszönni témavezetőmnek Dr. Fülöp József Andrásnak az útmutatását és a számos lehetőséget amit kaptam tőle, például, hogy már a BSc-s tanulmányaim végétől kezdve bevont a labormunkákba. Különösen hálás vagyok az ajánlásáért a SCIEX ösztöndíjra, ami lehetővé tette számomra, hogy több min egy évet tölthessek el a svájci Paul Scherrer Intézetben (PSI). Ahol próbára tehettem magam nemzetközi környezetben és új kapcsolatokat építhettem.

Szeretném megköszönni Prof. Dr. Christopher Hauri-nak a PSI-ből, hogy olyan vendégszeretően fogadott a csoportjában, valamint az útmutatását és az ötleteit a megvalósítandó kísérletről. Szeretném megköszönni Dr. Carlo Vicario-nak is az útmutatását és segítségét a laborban, különösképpen a lézerrendszer esetében, valamint a bevezetést az

for the measurements and calculations in Chapter 5.2.

I owe special thanks for two persons: Andrea Lóki, the managing expert of the Institute of Physics who helped me through the countless labyrinths of bureaucratic paperwork and for Andrew Cheesman from ELI-ALPS for the fast, last minute proofreading of my thesis.

I am also grateful for those colleagues and lab mates both at University and at PSI who provided me help and company during the long working hours and sometimes even after them.

Finally I would thank my family for getting me here. I am very grateful for all of their support, encouragement and patience what they provided me over the years of my life.

organikus kristályok világába. Köszönetet mondok Mojca Jazbinsek-nek is a Rainbow Photonics-tól az 5.2 fejezetben található mérésekért és számításokért.

Külön köszönet illet két személyt: Lóki Andreát a Fizikai Intézet ügyvivő szakértőjét, aki számtalanszor segített átjutni a bürokratikus papírmunka útvesztőin; valamint Andrew Cheesman-t az ELI-ALPS-ból a gyors, utolsó pillanatban elvégzett nyelvi lektorálásért.

Szintén hálást vagyok azoknak a kollégáknak és laboros társaknak mind az egyetem-en mind a PSI-nél akik segítséget és társaságot nyújtottak a hosszú munkaórák során és néha még az után is.

Végezetül szeretném megköszönni a családomnak, hogy eljuthattam idáig. Rendkívül hálás vagyok nekik mindazért a támogatásért, bátorításért és türelemért, amit nyújtottak nekem az életem évei alatt.

8. References

[1] W. Tu, S. Zhong, Y. Shen and A. Incecik, "Nondestructive testing of marine protective coatings using terahertz waves with stationary wavelet transform," *Ocean Engineering ,* vol. 111, pp. 582-592, 2016.

[2] S. Krimi, J. Klier, J. Jonuscheit, G. von Freymann, R. Urbansky and R. Beigang, "Highly accurate thickness measurement of multi-layered automotive paints using terahertz technology," *Applied Physics Letters,* vol. 109, no. 2, p. 021105, 2016.

[3] D. M. Hailu and D. Saeedkia, "Applications of Terahertz Technology for Plastic Industry," in *Advances in Imaging and Sensing*, Boca Raton, CRC Press, Taylor & Francis Group, 2017, pp. 107-117.

[4] C. Jördens and M. Koch, "Detection of foreign bodies in chocolate with pulsed terahertz spectroscopy," *Optical Engineering,* vol. 47, no. 3, pp. 037003-037003-5, 2008.

[5] Y.-K. LEE, S.-W. CHOI, S.-T. HAN, D. H. WOO and H. S. CHUN, "Detection of Foreign Bodies in Foods Using Continuous Wave Terahertz Imaging," *Journal of Food Protection,* vol. 75, no. 1, pp. 179-183, 2012.

[6] K. Kawase, Y. Ogawa, Y. Watanabe and H. Inoue, "Non-destructive terahertz imaging of illicit drugs using spectral fingerprints," *Opt. Express,* vol. 11, no. 20, pp. 2549-2554, Oct 2003.

[7] S. R. Murrill, E. L. Jacobs, S. K. Moyer, C. E. Halford, S. T. Griffin, F. C. D. Lucia, D. T. Petkie and C. C. Franck, "Terahertz imaging system performance model for concealed-weapon identification," *Appl. Opt.,* vol. 47, no. 9, pp. 1286-1297, Mar 2008.

[8] Y. C. Sim, J. Y. Park, K.-M. Ahn, C. Park and J.-H. Son, "Terahertz imaging of excised oral cancer at frozen temperature," *Biomed. Opt. Express,* vol. 4, no. 8, pp. 1413-1421, Aug 2013.

[9] F. Töpfer, S. Dudorov and J. Oberhammer, "Millimeter-Wave Near-Field Probe Designed for High-Resolution Skin Cancer Diagnosis," *IEEE Transactions on Microwave Theory and Techniques,* vol. 63, no. 6, pp. 2050-2059, June 2015.

[10] A. A. Angeluts, A. V. Balakin, M. D. Mishchenko, I. A. Ozheredov, M. N. Prokopchuk, T. N. Saphonova and A. P. Shkurinov, "Application of THz reflectometry to eye cornea hydration measurements," in *2016 41st International Conference on Infrared, Millimeter, and Terahertz waves (IRMMW-THz)*, 2016.

[11] F. Blanchard, D. Golde, F. H. Su, L. Razzari, G. Sharma, R. Morandotti, T. Ozaki, M. Reid, M. Kira, S. W. Koch and F. A. Hegmann, "Effective Mass Anisotropy of Hot Electrons in Nonparabolic Conduction Bands of n-Doped InGaAs Films Using Ultrafast Terahertz Pump-Probe Techniques," *Phys. Rev. Lett.,* vol. 107, p. 107401, Aug 2011.

[12] T. Kampfrath, K. Tanaka and K. A. Nelson, "Resonant and nonresonant control over matter and light by intense terahertz transients," *Nat. Photonics,* vol. 7, pp. 680-690, 2013.

[13] P. Gaal, K. Reimann, M. Woerner, T. Elsaesser, R. Hey and K. H. Ploog, "Nonlinear Terahertz Response of n-Type GaAs," *Phys. Rev. Lett.,* vol. 96, p. 187402, May 2006.

[14] T. Kampfrath, A. Sell, G. Klatt, A. Pashkin, S. Mahrlein, T. Dekorsy, M. Wolf, M. Fiebig, A. Leitenstorfer and R. Huber, "Coherent terahertz control of antiferromagnetic spin waves," *Nat Photon,* vol. 5, no. 1, pp. 31-34, #jan# 2011.

[15] J. Hebling, J. Fulop, M. Mechler, L. Palfalvi, C. Toke and others, "Optical Manipulation of Relativistic Electron Beams using THz Pulses," *arXiv,* Vols. -, p. 1109.6852, 2011.

[16] E. Balogh, K. Kovacs, P. Dombi, J. A. Fulop, G. Farkas, J. Hebling, V. Tosa and K. Varju, "Single attosecond pulse from terahertz-assisted high-order harmonic generation," *Phys. Rev. A,* vol. 84, p. 023806, Aug 2011.

[17] K. Kovács, E. Balogh, J. Hebling, V. Tosa and K. Varju, "Quasi-Phase-Matching High-Harmonic Radiation Using Chirped THz Pulses," *Phys. Rev. Lett.,* vol. 108, p. 193903, May 2012.

[18] W. R. Huang, E. A. Nanni, K. Ravi, K.-H. Hong, A. Fallahi, L. J. Wong, P. D. Keathley, L. E. Zapata and F. X. KÄ¤rtner, "Toward a terahertz-driven electron gun," *Scientific Reports,* vol. 5, pp. 14899--, #oct# 2015.

[19] E. A. Nanni, W. R. Huang, K.-H. Hong, K. Ravi, A. Fallahi, G. Moriena, R. J. Dwayne Miller and F. X. KÃ¤rtner, "Terahertz-driven linear electron acceleration," *Nature Communications,* vol. 6, pp. 8486--, #oct# 2015.

[20] Y.-S. Lee, Principles of Terahertz Science, New York: Springer Science+Business Media, LLC, 2009.

[21] G. W. Chantry, in *Long-wave Optics Vol. 2*, London, Academic Press, 1984, p. 574–576.

[22] G. Kozlov and A. Volkov, "Chap. 3.," in *Millimeter and Submillimeter Wave Spectroscopy of Solids*, Berlin, edited by G. Grüner, Springer-Verlag, 1998.

[23] C. Sirtori, S. Barbieri and R. Colombelli, "Wave engineering with THz quantum cascade lasers," *Nat Photon,* vol. 7, no. 9, pp. 691-701, #sep# 2013.

[24] M. A. Belkin and F. Capasso, "New frontiers in quantum cascade lasers: high performance room temperature terahertz sources," *Physica Scripta,* vol. 90, no. 11, p. 118002, 2015.

[25] Y. Bai, N. Bandyopadhyay, S. Tsao, S. Slivken and M. Razeghi, "Room temperature quantum cascade lasers with 27% wall plug efficiency," *Applied Physics Letters,* vol. 98, no. 18, p. 181102, 2011.

[26] S. Fathololoumi, E. Dupont, C. Chan, Z. Wasilewski, S. Laframboise, D. Ban, A. Mátyás, C. Jirauschek, Q. Hu and H. C. Liu, "Terahertz quantum cascade lasers

operating up to ~ 200 K with optimized oscillator strength and improved injection tunneling," *Opt. Express,* vol. 20, no. 4, pp. 3866-3876, Feb 2012.

[27] A. Wade, G. Fedorov, D. Smirnov, S. Kumar, S. Williams, Q. Hu and L. Reno, "Magnetic-field-assisted terahertz quantum cascade laser operating up to 225 K," *Nat Photon,* vol. 3, no. 1, pp. 41-45, #jan# 2009.

[28] B. Williams, S. Kumar, Q. Hu and J. Reno, "High-power terahertz quantum-cascade lasers," *Electronics Letters,* vol. 42, pp. 89-91(2), January 2006.

[29] L. Li, L. Chen, J. Zhu, J. Freeman, P. Dean, A. Valavanis, A. Davies and E. Linfield, "Terahertz quantum cascade lasers with >1 W output powers," *Electronics Letters,* vol. 50, pp. 309-311(2), February 2014.

[30] F. Wang, K. Maussang, S. Moumdji, R. Colombelli, J. R. Freeman, I. Kundu, L. Li, E. H. Linfield, A. G. Davies, J. Mangeney, J. Tignon and S. S. Dhillon, "Generating ultrafast pulses of light from quantum cascade lasers," *Optica,* vol. 2, no. 11, pp. 944-949, Nov 2015.

[31] D. Bachmann, M. Rosch, M. J. Suess, M. Beck, K. Unterrainer, J. Darmo, J. Faist and G. Scalari, "Short pulse generation and mode control of broadband terahertz quantum cascade lasers," *Optica,* vol. 3, no. 10, pp. 1087-1094, Oct 2016.

[32] A. Mottaghizadeh, D. Gacemi, P. Laffaille, H. Li, M. Amanti, C. Sirtori, G. Santarelli, W. Hansel, R. Holzwart, L. H. Li, E. H. Linfield and S. Barbieri, "5-ps-long terahertz pulses from an active-mode-locked quantum cascade laser," *Optica,* vol. 4, no. 1, pp. 168-171, Jan 2017.

[33] A. Abramovich, A. Arensburg, D. Chairman, A. Eichenbaum, M. Draznin, A. Gover, H. Kleinman, I. Merhasin, Y. Pinhasi, J. Sokolowski, Y. Yakover, M. Cohen, L. Levin, O. Shahal, A. Rosenberg, I. Schnitzer and J. Shiloh, "First operation of the Israeli Tandem Electrostatic Accelerator Free-Electron Laser," *Nuclear Instruments and Methods in Physics Research Section A: Accelerators, Spectrometers, Detectors and Associated Equipment ,* vol. 407, no. 1â€“3, pp. 16-20, 1998.

[34] Y. U. Jeong, G. M. Kazakevitch, H. J. Cha, S. H. Park and B. C. Lee, "Demonstration of a wide-band compact free electron laser to the THz imaging of bio samples," *Nuclear Instruments and Methods in Physics Research Section A: Accelerators, Spectrometers, Detectors and Associated Equipment ,* vol. 575, no. 1â€“2, pp. 58-62, 2007.

[35] T. Ping, H. Jiang, L. KaiFeng, X. YongQian and F. MingWu, "Terahertz radiation sources based on free electron lasers and their applications," *Science China Information Sciences,* vol. 55, no. 1, pp. 1-15, 2012.

[36] H. Hamster, A. Sullivan, S. Gordon, W. White and R. W. Falcone, "Subpicosecond, electromagnetic pulses from intense laser-plasma interaction," *Phys. Rev. Lett.,* vol. 71, pp. 2725-2728, Oct 1993.

[37] D. J. Cook and R. M. Hochstrasser, "Intense terahertz pulses by four-wave rectification in air," *Opt. Lett.,* vol. 25, no. 16, pp. 1210-1212, Aug 2000.

[38] M. Kress, T. Löffler, S. Eden, M. Thomson and H. G. Roskos, "Terahertz-pulse generation by photoionization of air with laser pulses composed of both

fundamental and second-harmonic waves," *Opt. Lett.,* vol. 29, no. 10, pp. 1120-1122, May 2004.

[39] T. Bartel, P. Gaal, K. Reimann, M. Woerner and T. Elsaesser, "Generation of single-cycle THz transients with high electric-field amplitudes," *Opt. Lett.,* vol. 30, no. 20, pp. 2805-2807, Oct 2005.

[40] J. Xie, W.-H. Fan and X. Chen, "Systematic experimental study on a highly efficient terahertz source based on two-color laser-induced air plasma," *Laser Physics,* vol. 26, no. 5, p. 055002, 2016.

[41] T. I. Oh, Y. S. You, N. Jhajj, E. W. Rosenthal, H. M. Milchberg and K. Y. Kim, "Scaling and saturation of high-power terahertz radiation generation in two-color laser filamentation," *Applied Physics Letters,* vol. 102, no. 20, 2013.

[42] D. Kuk, Y. J. Yoo, E. W. Rosenthal, N. Jhajj, H. M. Milchberg and K. Y. Kim, "Generation of scalable terahertz radiation from cylindrically focused two-color laser pulses in air," *Applied Physics Letters,* vol. 108, no. 12, p. 121106, 2016.

[43] I.-C. Ho, X. Guo and X.-C. Zhang, "Design and performance of reflective terahertz air-biased-coherent-detection for time-domain spectroscopy," *Opt. Express,* vol. 18, pp. 2872-2883, Feb 2010.

[44] N. Karpowicz, J. Dai, X. Lu, Y. Chen, M. Yamaguchi, H. Zhao, X.-C. Zhang, L. Zhang, C. Zhang, M. Price-Gallagher, C. Fletcher, O. Mamer, A. Lesimple and K. Johnson, "Coherent heterodyne time-domain spectrometry covering the entire “terahertz gap”," *Applied Physics Letters,* vol. 92, no. 1, p. 011131, 2008.

[45] C. W. Berry, M. R. Hashemi and M. Jarrahi, "Generation of high power pulsed terahertz radiation using a plasmonic photoconductive emitter array with logarithmic spiral antennas," *Applied Physics Letters,* vol. 104, no. 8, p. 081122, 2014.

[46] L. Luo, I. Chatzakis, J. Wang, F. B. P. Niesler, M. Wegener, T. Koschny and C. M. Soukoulis, "Broadband terahertz generation from metamaterials," *Nature Communications,* vol. 5, pp. 3055--, #jan# 2014.

[47] R. W. Boyd, Nonlinear Optics (Third Edition), Academic Press (Elsevier), 2008.

[48] P. A. Franken, A. E. Hill, C. W. Peters and G. Weinreich, "Generation of Optical Harmonics," *Phys. Rev. Lett.,* vol. 7, pp. 118-119, Aug 1961.

[49] M. Bass, P. A. Franken, A. E. Hill, C. W. Peters and G. Weinreich, "Optical Mixing," *Phys. Rev. Lett.,* vol. 8, pp. 18-18, Jan 1962.

[50] M. Bass, P. A. Franken, J. F. Ward and G. Weinreich, "Optical Rectification," *Phys. Rev. Lett.,* vol. 9, pp. 446-448, Dec 1962.

[51] M. Garfinkel and W. E. Engeler, "SUM FREQUENCIES AND HARMONIC GENERATION IN GaAs LASERS," *Applied Physics Letters,* vol. 3, no. 10, pp. 178-180, 1963.

[52] J. A. Armstrong, N. Bloembergen, J. Ducuing and P. S. Pershan, "Interactions between Light Waves in a Nonlinear Dielectric," *Phys. Rev.,* vol. 127, pp. 1918-1939, Sep 1962.

[53] G. D. Boyd, A. Ashkin, J. M. Dziedzic and D. A. Kleinman, "Second-Harmonic Generation of Light with Double Refraction," *Phys. Rev.,* vol. 137, pp. A1305--A1320, Feb 1965.

[54] L. E. Myers, W. R. Bosenberg, G. D. Miller, R. C. Eckardt, M. M. Fejer and R. L. Byer, "Quasi-phase-matched 1.064-µm-pumped optical parametric oscillator in bulk periodically poled LiNbO3," *Opt. Lett.,* vol. 20, no. 1, pp. 52-54, Jan 1995.

[55] L. E. Myers, R. C. Eckardt, M. M. Fejer, R. L. Byer, W. R. Bosenberg and J. W. Pierce, "Quasi-phase-matched optical parametric oscillators in bulk periodically poled LiNbO3," *J. Opt. Soc. Am. B,* vol. 12, no. 11, pp. 2102-2116, Nov 1995.

[56] J. Hebling, G. Almási, I. Z. Kozma and J. Kuhl, "Velocity matching by pulse front tilting for large-area THz-pulse generation," *Opt. Express,* vol. 10, no. 21, pp. 1161-1166, Oct 2002.

[57] H. H. Li, "Refractive Index of ZnS, ZnSe, and ZnTe and Its Wavelength and Temperature Derivatives," *Journal of Physical and Chemical Reference Data,* vol. 13, no. 1, pp. 103-150, 1984.

[58] W. L. Bond, "Measurement of the Refractive Indices of Several Crystals," *Journal of Applied Physics,* vol. 36, no. 5, pp. 1674-1677, 1965.

[59] T. Skauli, P. S. Kuo, K. L. Vodopyanov, T. J. Pinguet, O. Levi, L. A. Eyres, J. S. Harris, M. M. Fejer, B. Gerard, L. Becouarn and E. Lallier, "Improved dispersion relations for GaAs and applications to nonlinear optics," *Journal of Applied Physics,* vol. 94, no. 10, pp. 6447-6455, 2003.

[60] M. Schall, M. Walther and P. Uhd Jepsen, "Fundamental and second-order phonon processes in CdTe and ZnTe," *Phys. Rev. B,* vol. 64, p. 094301, Aug 2001.

[61] D. F. Parsons and P. D. Coleman, "Far Infrared Optical Constants of Gallium Phosphide," *Appl. Opt.,* vol. 10, no. 7, pp. 1683_1--1685, Jul 1971.

[62] N. Katzenellenbogen and D. Grischkowsky, "Electrical characterization to 4 THz of N- and P-type GaAs using THz time-domain spectroscopy," *Applied Physics Letters,* vol. 61, no. 7, pp. 840-842, 1992.

[63] J. Hebling, K.-L. Yeh, M. C. Hoffmann, B. Bartal and K. A. Nelson, "Generation of high-power terahertz pulses by tilted-pulse-front excitation and their application possibilities," *J. Opt. Soc. Am. B,* vol. 25, no. 7, pp. B6--B19, Jul 2008.

[64] Q. Wu and X.-C. Zhang, "Ultrafast electro-optic field sensor," *Applied Physics Letters,* vol. 68, no. 12, pp. 1604-1606, 1996.

[65] J. Hebling, A. Stepanov, G. Almasi, B. Bartal and J. Kuhl, "Tunable THz pulse generation by optical rectification of ultrashort laser pulses with tilted pulse fronts," *Applied Physics B,* vol. 78, no. 5, pp. 593-599, 2004.

[66] F. Blanchard, L. Razzari, H. Bandulet, G. Sharma, R. Morandotti, J. C. Kieffer, T. Ozaki, M. Reid, H. F. Tiedje, H. K. Haugen and F. A. Hegmann, "Generation of 1.5uJ single-cycle terahertz pulses by optical rectification from a large aperture ZnTe crystal," *Opt. Express,* vol. 15, no. 20, pp. 13212-13220, Oct 2007.

[67] M. C. Hoffmann, K.-L. Yeh, J. Hebling and K. A. Nelson, "Efficient terahertz generation by optical rectification at 1035 nm," *Opt. Express,* vol. 15, p. 11706, 2007.

[68] F. Blanchard, B. E. Schmidt, X. Ropagnol, N. Thire, T. Ozaki, R. Morandotti, D. G. Cooke and F. Legare, "Terahertz pulse generation from bulk GaAs by a tilted-pulse-front excitation at 1.8 μm," *Applied Physics Letters,* vol. 105, no. 24, 2014.

[69] J. A. Fülöp, G. Polónyi, B. Monoszlai, G. Andriukaitis, T. Balciunas, A. Pugzlys, G. Arthur, A. Baltuska and J. Hebling, "Highly efficient scalable monolithic semiconductor terahertz pulse source," *Optica,* vol. 3, no. 10, pp. 1075-1078, Oct 2016.

[70] G. Polónyi, B. Monoszlai, G. Gäumann, E. J. Rohwer, G. Andriukaitis, T. Balciunas, A. Pugzly, A. Baltuska, T. Feurer, J. Hebling and J. A. Fülöp, "High-energy terahertz pulses from semiconductors pumped beyond the three-photon absorption edge," *Opt. Express,* vol. 24, no. 21, pp. 23872-23882, Oct 2016.

[71] L. Pálfalvi, J. Hebling, G. Almási, Á. Péter, K. Polgár, K. Lengyel and R. Szipöcs, "Nonlinear refraction and absorption of Mg doped stoichiometric and congruent LiNbO3," *Journal of Applied Physics,* vol. 95, no. 3, pp. 902-908, 2004.

[72] X. Wu, C. Zhou, W. R. Huang, F. Ahr and F. X. Kartner, "Temperature dependent refractive index and absorption coefficient of congruent lithium niobate crystals in the terahertz range," *Opt. Express,* vol. 23, no. 23, pp. 29729-29737, Nov 2015.

[73] O. Gayer, Z. Sacks, E. Galun and A. Arie, "Temperature and wavelength dependent refractive index equations for MgO-doped congruent and stoichiometric LiNbO3," *Applied Physics B,* vol. 91, no. 2, pp. 343-348, 2008.

[74] L. Pálfalvii, J. Hebling, J. Kuhl, Á. Péter and K. Polgár, "Temperature dependence of the absorption and refraction of Mg-doped congruent and stoichiometric LiNbO3 in the THz range," *Journal of Applied Physics,* vol. 97, no. 12, p. 123505, 2005.

[75] M. Schall, H. Helm and S. R. Keiding, "Far Infrared Properties of Electro-Optic Crystals Measured by THz Time-Domain Spectroscopy," *International Journal of Infrared and Millimeter Waves,* vol. 20, no. 4, pp. 595-604, 1999.

[76] A. G. Stepanov, S. Henin, Y. Petit, L. Bonacina, J. Kasparian and J.-P. Wolf, "Mobile source of high-energy single-cycle terahertz pulses," *Applied Physics B,* vol. 101, no. 1, pp. 11-14, 2010.

[77] J. A. Fülöp, Z. Ollmann, C. Lombosi, C. Skrobol, S. Klingebiel, L. Pálfalvi, F. Krausz, S. Karsch and J. Hebling, "Efficient generation of THz pulses with 0.4 mJ energy," *Opt. Express,* vol. 22, no. 17, pp. 20155-20163, Aug 2014.

[78] C. Ruchert, C. Vicario and C. P. Hauri, "Scaling submillimeter single-cycle transients toward megavolts per centimeter field strength via optical rectification in the organic crystal OH1," *Opt. Lett.,* vol. 37, pp. 899-901, Mar 2012.

[79] C. P. Hauri, C. Ruchert, C. Vicario and F. Ardana, "Strong-field single-cycle THz pulses generated in an organic crystal," *Applied Physics Letters,* vol. 99, no. 16, p. 161116, 2011.

[80] C. Vicario, B. Monoszlai, M. Jazbinsek, S. H. Lee, O. P. Kwon and C. P. Hauri, "Intense, carrier frequency and bandwidth tunable quasi single-cycle pulses from an organic emitter covering the Terahertz frequency gap," *Scientific Reports,* vol. 5, pp. 14394--, #sep# 2015.

[81] C. Vicario, A. V. Ovchinnikov, S. I. Ashitkov, M. B. Agranat, V. E. Fortov and C. P. Hauri, "Generation of 0.9-mJ THz pulses in DSTMS pumped by a Cr:Mg2SiO4 laser," *Opt. Lett.,* vol. 39, pp. 6632-6635, Dec 2014.

[82] X.-C. Zhang, X. F. Ma, Y. Jin, T.-M. Lu, E. P. Boden, P. D. Phelps, K. R. Stewart and C. P. Yakymyshyn, "Terahertz optical rectification from a nonlinear organic crystal," *Applied Physics Letters,* vol. 61, no. 26, pp. 3080-3082, 1992.

[83] R. P. AG, "Rainbow Photonics," http://www.rainbowphotonics.com/, [Online]. Available: http://www.rainbowphotonics.com/prod_dast.php. [Accessed 16 11 2016].

[84] Y. Hosokawa, H. Adachi, M. Yoshimura, Y. Mori, T. Sasaki and H. Masuhara, "Femtosecond Laser-Induced Crystallization of 4-(Dimethylamino)-N-methyl-4-stilbazolium Tosylate," *Crystal Growth & Design,* vol. 5, no. 3, pp. 861-863, 2005.

[85] C. Bosshard, K. Sutter, P. Prêtre, J. Hulliger, M. Flörsheimer, P. Kaatz and P. Günter, "Organic Nonlinear Optical Materials," in *Advances in Nonlinear Optics Vol. 1*, Amsterdam, Gordon and Breach, 1995.

[86] A. Schneider, "Generation and detection of terahertz pulses in organic crystals," in *PhD thesis*, Zürich, Swiss Federal Institute of Technology, 2005.

[87] L. Mutter, M. Jazbinšek, M. Zgonik, U. Meier, C. Bosshard and P. Günter, "Photobleaching and optical properties of organic crystal 4-N, N-dimethylamino-4'-N'-methyl stilbazolium tosylate," *Journal of Applied Physics,* vol. 94, no. 3, pp. 1356-1361, 2003.

[88] K. Nagaoka, H. Adachi, S. Brahadeeswaran, T. Higo, M. Takagi, M. Yoshimura, Y. Mori and T. Sasaki, "Controlled Habit and Growth, and Electrooptic Evaluation of Organic Nonlinear Optical 4-Dimethylamino- N -Methyl-4-Stilbazolium Tosylate (DAST) Crystals," *Japanese Journal of Applied Physics,* vol. 43, no. 2B, p. L261, 2004.

[89] S. Manetta, M. Ehrensperger, C. Bosshard and P. Günter, "Organic thin film crystal growth for nonlinear optics: present methods and exploratory developments," *Comptes Rendus Physique,* vol. 3, no. 4, pp. 449-462, 2002.

[90] F. Pan, G. Knöpfle, C. Bosshard, S. Follonier, R. Spreiter, M. S. Wong and P. Günter, "Electro-optic properties of the organic salt 4-N,N-dimethylamino-4'-N'-methyl-stilbazolium tosylate," *Applied Physics Letters,* vol. 69, no. 1, pp. 13-15, 1996.

[91] P. D. Cunningham and L. M. Hayden, "Optical properties of DAST in the THz range," *Opt. Express,* vol. 18, no. 23, pp. 23620-23625, Nov 2010.

[92] Z. Yang, L. Mutter, M. Stillhart, B. Ruiz, S. Aravazhi, M. Jazbinsek, A. Schneider, V. Gramlich and P. Günter, "Large-Size Bulk and Thin-Film Stilbazolium-Salt Single Crystals for Nonlinear Optics and THz Generation," *Advanced Functional Materials,* vol. 17, no. 13, pp. 2018-2023, 2007.

[93] L. Mutter, F. D. Brunner, Z. Yang, M. Jazbinšek and P. Günter, "Linear and nonlinear optical properties of the organic crystal DSTMS," *J. Opt. Soc. Am. B,* vol. 24, no. 9, pp. 2556-2561, Sep 2007.

[94] J. C. Brice, Crystal Growth Process, New York: Wiley, 1996.

[95] C. Vicario, B. Monoszlai and C. P. Hauri, "GV/m Single-Cycle Terahertz Fields from a Laser-Driven Large-Size Partitioned Organic Crystal," *Phys. Rev. Lett.,* vol. 112, p. 213901, May 2014.

[96] M. Stillhart, A. Schneider and P. Günter, "Optical properties of 4-N,N-dimethylamino- 4'-N'4'-N' -methyl-stilbazolium 2,4,6-trimethylbenzenesulfonate crystals at terahertz frequencies," *J. Opt. Soc. Am. B,* vol. 25, no. 11, pp. 1914-1919, Nov 2008.

[97] U. Meier, M. Bösch, C. Bosshard, F. Pan and P. Günter, "Parametric interactions in the organic salt 4-N,N4-N,N-dimethylamino-4'-N'4'-N'- methyl-stilbazolium tosylate at telecommunication wavelengths," *Journal of Applied Physics,* vol. 83, no. 7, pp. 3486-3489, 1998.

[98] P. L. Richards, "Bolometers for infrared and millimeter waves," *Journal of Applied Physics,* vol. 76, no. 1, pp. 1-24, 1994.

[99] H. P. Beerman, "The pyroelectric detector of infrared radiation," *IEEE Transactions on Electron Devices,* vol. 16, no. 6, pp. 554-557, Jun 1969.

[100] M. J. E. Golay, "The Theoretical and Practical Sensitivity of the Pneumatic Infra-Red Detector," *Review of Scientific Instruments,* vol. 20, no. 11, pp. 816-820, 1949.

[101] J. B. Chévrier, K. Baert, T. Slater and A. Verbist, "Micromachined infrared pneumatic detector for gas sensor," *Microsystem Technologies,* vol. 1, no. 2, pp. 71-74, 1995.

[102] T. W. Kenny, W. J. Kaiser, S. B. Waltman and J. K. Reynolds, "Novel infrared detector based on a tunneling displacement transducer," *Applied Physics Letters,* vol. 59, no. 15, pp. 1820-1822, 1991.

[103] D. T. Nguyen, F. Simoens, J. L. Ouvrier-Buffet, J. Meilhan and J. L. Coutaz, "Broadband THz Uncooled Antenna-Coupled Microbolometer Array - Electromagnetic Design, Simulations and Measurements," *IEEE Transactions on Terahertz Science and Technology,* vol. 2, no. 3, pp. 299-305, May 2012.

[104] J. Yang, S. Ruan and M. Zhang, "Real-time, continuous-wave terahertz imaging by a pyroelectric camera," *Chin. Opt. Lett.,* vol. 6, no. 1, pp. 29-31, Jan 2008.

[105] N. Nemoto, N. Kanda, R. Imai, K. Konishi, M. Miyoshi, S. Kurashina, T. Sasaki, N. Oda and M. Kuwata-Gonokami, "High-Sensitivity and Broadband, Real-Time Terahertz Camera Incorporating a Micro-Bolometer Array With Resonant Cavity Structure," *IEEE Transactions on Terahertz Science and Technology,* vol. 6, no. 2, pp. 175-182, March 2016.

[106] N. Kanda, K. Konishi, N. Nemoto, K. Midorikawa and M. Kuwata-Gonokami, "Real-time broadband terahertz spectroscopic imaging by using a high-sensitivity terahertz camera," *Scientific Reports,* vol. 7, pp. 42540--, #feb# 2017.

[107] G. Gallot and D. Grischkowsky, "Electro-optic detection of terahertz radiation," *J. Opt. Soc. Am. B,* vol. 16, no. 8, pp. 1204-1212, Aug 1999.

[108] A. Trisorio, P. M. Paul, F. Ple, C. Ruchert, C. Vicario and C. P. Hauri, "Ultrabroadband TW-class Ti:sapphire laser system with adjustable central wavelength, bandwidth and multi-color operation," *Opt. Express,* vol. 19, no. 21, pp. 20128-20140, Oct 2011.

[109] B. Monoszlai, C. Vicario, M. Jazbinsek and C. P. Hauri, "High-energy terahertz pulses from organic crystals: DAST and DSTMS pumped at Ti:sapphire wavelength," *Opt. Lett.,* vol. 38, no. 23, pp. 5106-5109, Dec 2013.

[110] A. Schneider, M. Neis, M. Stillhart, B. Ruiz, R. U. A. Khan, P. Günter and A. Schneider, "Generation of terahertz pulses through optical rectification in organic DAST crystals: theory and experiment," *JOSA B,* vol. 23, no. 9, pp. 1822-1835, 2006.

[111] X. Zheng, C. V. McLaughlin, P. Cunningham and L. M. Hayden, "Organic Broadband TeraHertz Sources and Sensors," *J. Nanoelectron. Optoelectron.,* vol. 2, no. 2, pp. 58-76, 2007.

[112] A. Trisorio, M. Divall, B. Monoszlai, C. Vicario and C. P. Hauri, "Intense sub-two-cycle infrared pulse generation via phase-mismatched cascaded nonlinear interaction in DAST crystal," *Opt. Lett.,* vol. 39, no. 9, pp. 2660-2663, May 2014.

[113] C. Vicario, B. Monoszlai, G. Arisholm and C. P. Hauri, "Generation of 1.5-octave intense infrared pulses by nonlinear interactions in DAST crystal," *Journal of Optics,* vol. 17, no. 9, p. 094005, 2015.

[114] C. Vicario, C. Ruchert, F. Ardana-Lamas, P. M. Derlet, B. Tudu, C. P. Hauri and J. Luning, "Off-resonant magnetization dynamics phase-locked to an intense phase-stable terahertz transient," *Nat. Photon.,* vol. 7, p. 720–723, 2013.

[115] M. Shalaby and C. P. Hauri, "Demonstration of a low-frequency three-dimensional terahertz bullet with extreme brightness," *Nat Commun,* vol. 6, no. 5976, pp. --, #jan# 2015.

[116] M. Kunitski, M. Richter, M. D. Thomson, A. Vredenborg, J. Wu, T. Jahnke, M. Schöffler, H. Schmidt-Böcking, H. G. Roskos and R. Dörner, "Optimization of single-cycle terahertz generation in LiNbO3 for sub-50 femtosecond pump pulses," *Opt. Express,* vol. 21, no. 6, pp. 6826-6836, Mar 2013.

[117] C. Ruchert, C. Vicario and C. P. Hauri, "Spatiotemporal Focusing Dynamics of Intense Supercontinuum THz Pulses," *Phys. Rev. Lett.,* vol. 110, p. 123902, Mar 2013.

[118] S. Feng, H. G. Winful and R. W. Hellwarth, "Gouy shift and temporal reshaping of focused single-cycle electromagnetic pulses," *Opt. Lett.,* vol. 23, no. 5, pp. 385-387, Mar 1998.

[119] A. B. Ruffin, J. V. Rudd, J. F. Whitaker, S. Feng and H. G. Winful, "Direct Observation of the Gouy Phase Shift with Single-Cycle Terahertz Pulses," *Phys. Rev. Lett.,* vol. 83, pp. 3410-3413, Oct 1999.

[120] K. L. Vodopyanov, "Optical generation of narrow-band terahertz packets in periodically-inverted electro-optic crystals: conversion efficiency and optimal laser pulse format," *Opt. Express,* vol. 14, no. 6, pp. 2263-2276, Mar 2006.

[121] R. DeSalvo, D. J. Hagan, M. Sheik-Bahae, G. Stegeman, E. W. V. Stryland and H. Vanherzeele, "Self-focusing and self-defocusing by cascaded second-order effects in KTP," *Opt. Lett.,* vol. 17, no. 1, pp. 28-30, Jan 1992.

[122] B. B. Zhou, A. Chong, F. W. Wise and M. Bache, "Ultrafast and Octave-Spanning Optical Nonlinearities from Strongly Phase-Mismatched Quadratic Interactions," *Phys. Rev. Lett.,* vol. 109, p. 043902, Jul 2012.

[123] T. Popmintchev, M.-C. Chen, D. Popmintchev, P. Arpin, S. Brown, S. Ališauskas, G. Andriukaitis, T. Balčiunas, O. D. Mücke, A. Pugzlys, A. Baltuška, B. Shim, S. E. Schrauth, A. Gaeta, C. Hernández-García, L. Plaja, A. Becker, A. Jaron-Becker, M. M. Murnane and H. C. Kapteyn, "Bright Coherent Ultrahigh Harmonics in the keV X-ray Regime from Mid-Infrared Femtosecond Lasers," *Science,* vol. 336, no. 6086, pp. 1287-1291, 2012.

[124] G. Lu and B. Fei, "Medical hyperspectral imaging: a review," *Journal of Biomedical Optics,* vol. 19, no. 1, p. 010901, 2014.

[125] G. Gitzinger, "Multi-octave acousto-optic spectrum analyzer for mid-infrared pulsed sources," in *CLEO: OSA Technical Digest paper STh1N.5*, 2014.

[126] A. Trisorio, S. Grabielle, M. Divall, N. Forget and C. P. Hauri, "Self-referenced spectral interferometry for ultrashort infrared pulse characterization," *Opt. Lett.,* vol. 37, no. 14, pp. 2892-2894, Jul 2012.

[127] C. Bosshard, I. Biaggio, S. Fischer, S. Follonier and P. Günter, "Cascaded contributions to degenerate four-wave mixing in an acentric organic crystal," *Opt. Lett.,* vol. 24, no. 4, pp. 196-198, Feb 1999.

[128] A. Schneider, I. Biaggio and P. Gunter, "Terahertz-induced lensing and its use for the detection of terahertz pulses in a birefringent crystal," *Applied Physics Letters,* vol. 84, no. 13, pp. 2229-2231, 2004.